12-1-2015

Chemical and Electronic Structure of Surfaces and Interfaces in Cadmium Telluride Based Photovoltaic Devices

Douglas Arthur Duncan
University of Nevada, Las Vegas, douglashanks@me.com

CHEMICAL AND ELECTRONIC STRUCTURE OF SURFACES

AND INTERFACES IN CADMIUM TELLURIDE

BASED PHOTOVOLTAIC DEVICES

by

Douglas Arthur Duncan

Bachelor of Science – Chemistry
University of Nevada, Las Vegas
2010

A dissertation submitted in partial fulfillment
of the requirements for the

Doctor of Philosophy – Chemistry

Department of Chemistry and Biochemistry
College of Sciences
The Graduate College

University of Nevada, Las Vegas
December 2015

UNLV | GRADUATE COLLEGE

Dissertation Approval

The Graduate College
The University of Nevada, Las Vegas

September 23, 2015

This dissertation prepared by

Douglas Arthur Duncan

entitled

Chemical and Electronic Structure of Surfaces and Interfaces in Cadmium Telluride Based Photovoltaic Devices

is approved in partial fulfillment of the requirements for the degree of

Doctor of Philosophy – Chemistry
Department of Chemistry and Biochemistry

Clemens Heske, Ph.D.
Examination Committee Chair

Kathleen Robins, Ph.D.
Examination Committee Member

Dong-Chan Lee, Ph.D.
Examination Committee Member

Rama Venkat, Ph.D.
Graduate College Faculty Representative

Kathryn Hausbeck Korgan, Ph.D.
Graduate College Interim Dean

ABSTRACT

CHEMICAL AND ELECTRONIC STRUCTURE OF SURFACE

AND INTERFACES IN CADMIUM TELLURIDE

BASED PHOTOVOLTAIC DEVICES

by

Douglas Arthur Duncan

Dr. Clemens Heske, Examination Committee Chair
Professor of Chemistry
University of Nevada, Las Vegas

The surface and interface properties are of the upmost importance in the understanding, optimization, and application for photovoltaic devices. Often the chemical, electronic, and morphological properties of the films are empirically optimized, however when progress slows, a fundamental understanding of these properties can lead to breakthroughs. In this work, surfaces and interfaces of solar cell-relevant films are probed with a repertoire of X-ray analytical and microanalysis techniques including X-ray photoelectron (XPS), X-ray excited Auger electron (XAES), X-ray emission (XES) spectroscopies, and atomic force (AFM) and scanning electron (SEM) microscopies.

Silicon-based devices currently dominate the solar market, which is rather inflexible in application. Cadmium telluride (CdTe)-based technologies offer a cost-effective alternative with additional benefits including roll-to-roll production and high conversion efficiencies. This, like other next generation thin film solar cells, needs more optimization to replace Si. The charge transport across a heterojunction is of great importance to drive up the conversion efficiency of the device.

The interface of a CdS buffer layer and SnO_2:F front contact was investigated as a function of $CdCl_2$-treatment. In order to measure the fully formed interface, after subsequent layer deposition and heat treatments, mechanical stressing of the layer stack resulted in physical separation at the desired interface. By combining multiple spectroscopic and morphologic methods a complete picture has evolved.

CdS is often used as a buffer layer in CdTe based devices. This layer is empirically optimized to be very thin (~100 nm) due to the parasitic light absorption in and around the 2 eV range. By widening the band gap or replacing it with a more transparent material, more photons can be absorbed by the CdTe layer and significantly increase the overall conversion efficiency of the device. CdS:O and $Zn_{(1-x)}Mg_xO$ were studied as possible alternatives to CdS. The chemical composition of CdS:O was studied at the surface and bulk of the film with respect to oxygen content. The interfacial properties of $SnO_2/Zn_{(1-x)}Mg_xO$ and $Zn_{(1-x)}Mg_xO/CdTe$ were also investigated with particular emphasis on energy level alignments at the interfaces.

ACKNOWLEDGEMENTS

TABLE OF CONTENTS

LIST OF FIGURES

CHAPTER 1   INTRODUCTION

1.1 Motivation

CdTe-based solar cells have reached efficiencies of up to 20.4% in the laboratory (small area) scale, 17.0% for modules (large area)[1]. These values have been improving at a rapid rate over the past 4 years (Figure 1.1). To further improve CdTe technology a fundamental understanding of chemical and electron properties is important. Furthermore many studies use academic sample sets, which do not completely describe a real world device. In this work we bridge the informational gap between fundamental research and real world devices.
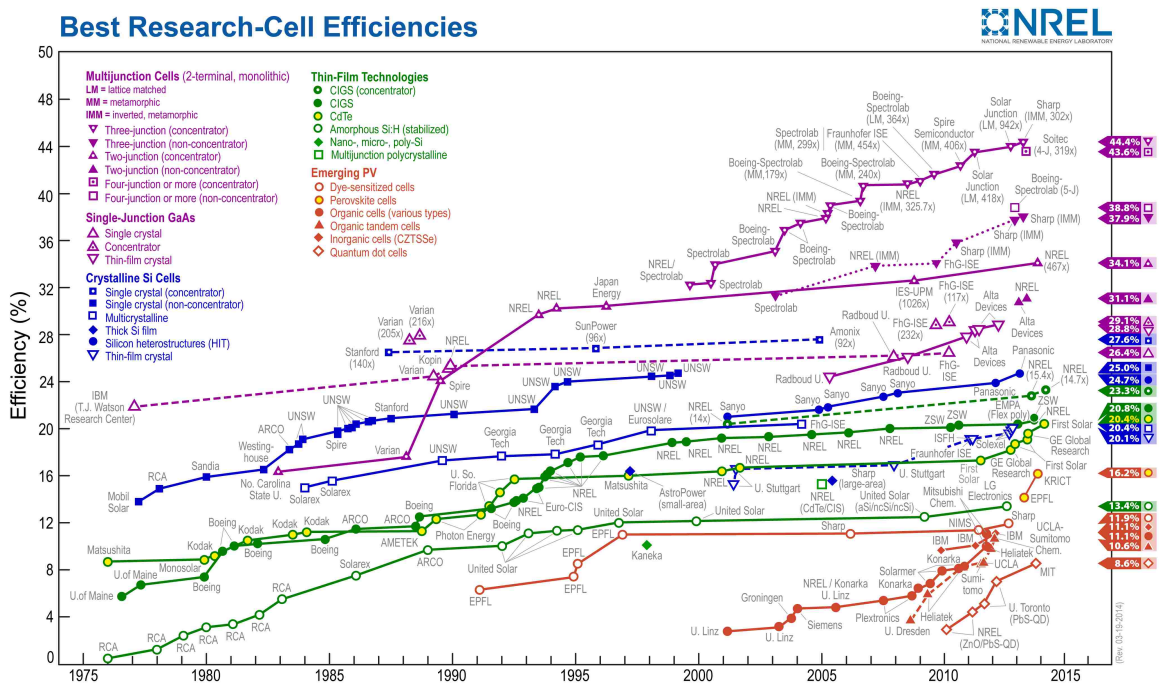
Figure 1.1: Record research cell efficiency organized by technology

1.2 Dissertation Organization

Surface-sensitive photoelectron spectroscopy is an ideal tool to study the electronic and chemical properties of surfaces and interfaces, including interfacial band

gaps and band offsets in the valence and conduction band. However, before such surface-sensitive methods can be employed, surface adsorbates or oxides, which can significantly skew the results, need to be removed. Chapter 4 studies the impact of a low-energy ion surface treatment on the electronic and chemical surface properties of an air-exposed CdTe thin film, monitoring the effectiveness and suitability of such surface cleaning for the preparation of relevant CdTe thin-film surfaces and interfaces.

To further improve performance, a fundamental understanding of the chemical and electronic interface structure throughout the $CdCl_2$-treated $CdTe/CdS/SnO_2$:F/glass layer stack is necessary. Significant diffusion processes occur during manufacturing, particularly these induced by the post-deposition $CdCl_2$ treatment. Thus, most interfaces in the device are not fully formed until after these treatments, presenting a challenge to standard surface-science characterization approaches of step-wise material deposition.

In Chapter 5, we probe the buried CdS/SnO_2:F interface using a combination of surface-sensitive characterization methods and a reproducible cleaving process, which was achieved by gluing metal sheets to both sides of the layer stack to allow for a mechanical lift-off in an inert environment. To investigate the morphological, chemical, and electronic properties of the exposed surfaces after lift-off, atomic force microscopy (AFM), X-ray (XPS) and ultra-violet (UPS) photoelectron spectroscopy, as well as inverse photoemission spectroscopy (IPES) was used.

In Chapter 6, efforts focus on the fact that absorption in the CdS buffer layer of such cells reduces the flux of high-energy photons to the CdTe absorber. This parasitic light absorption can result in more than 10% loss in short-circuit current density.[2] One way to prevent this loss is to increase the band gap of the buffer material, e.g., by

incorporating oxygen during RF sputtering of CdS (such as by introducing O_2 into the Ar flow).[3-7] This process has produced devices with efficiencies above 15%.[3, 5, 8] To analyze the chemical structure of the S in detail, x-ray photoelectron spectroscopy (XPS) and soft x-ray emission spectroscopy (XES) were used to study the species-specific composition of the surface and bulk, respectively. Thus the impact of oxygen incorporation into CdS thin films is derived, by monitoring the relative intensities of the various sulfur species at the surface and bulk as a function of O content. The results allow for deeper insights into, and deliberate optimization of, such CdS:O thin films in solar devices.

In Chapter 7 & 8, efforts continue on reducing parasitic light absorption, but in this case together with First Solar Inc. CdS is completely replaced with $Zn_{(1-x)}Mg_xO$ or (Zn,Mg)O. Both interfaces of the (Zn,Mg)O (SnO_2/(Zn,Mg)O and (Zn,Mg)O/CdTe) are studied to find the chemical composition and the band alignment at the interface.

CHAPTER 2 LITERATURE REVIEW

2.1 Heterojunction Formation in Solar Cells

A solar cell diode is constructed of a p-n junction. The junction is formed when two materials (shown in Figure 2.1a), with the Fermi level (E_F) near the valence band of one and the conduction band of the other are joined. In order to reach thermal equilibrium the E_F must be equal energies for both materials (Figure 2.1b). The p-n junction may be formed from similar materials (homojunction), as is the case for silicon, or dissimilar materials (heterojunction) like CdTe/CdS devices.
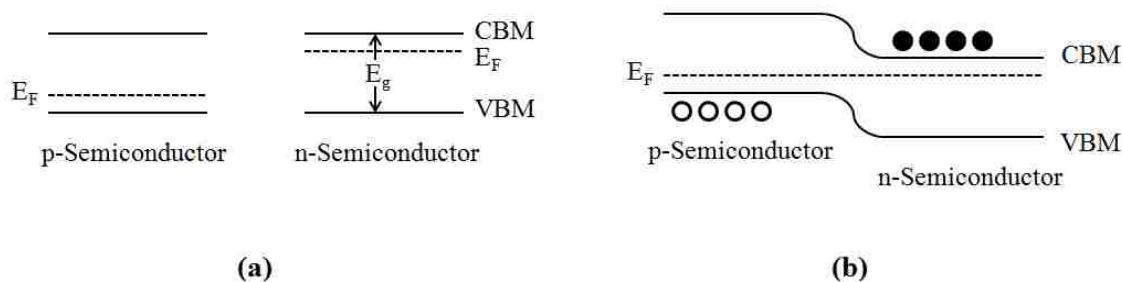
Figure 2.1: A p-type and n-type semiconductor (a) independently, and (b) joined and in thermal equilibrium with majority carriers shown. (adapted from [9])

The typical device structure is shown in Figure 2.2. The front contact, normally SnO_2:F, is between the n-type CdS and the glass substrate. Both the front contact and glass substrate should be transparent to photon energies that can contribute to photocurrent. When sunlight ($h\nu \geq E_g$) impinges on the device, electrons are excited from the valence band to the conduction band and leaves behind 'holes'. The excited electrons move to the front contact, while holes move in the opposite direction and are collected at the back contact, which is usually a metal (e.g., Cu, Au, Al, etc.).
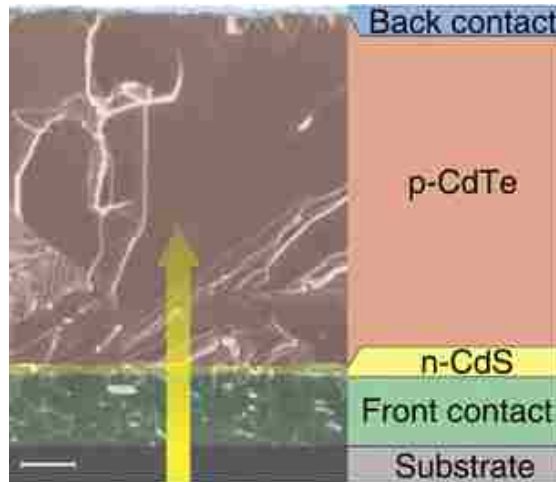
Figure 2.2: Scanning electron micrograph and schematic of the cross-section of a CdTe solar cell, the direction of light is shown by a yellow arrow. (adapted from [10])

One variable that needs to be optimized for a solar cell is the electronic level alignment at various interfaces. The interface plays a dominant role in the current output (J_{sc}) and is often a focus of optimization. The conduction band (CB) alignment is important for the transport of photogenerated electrons to the front contact. There are three configurations for the CB to align in this heterojunction: "spike," "flat," or "cliff" configurations, which are shown schematically shown in Fig. 2.3.
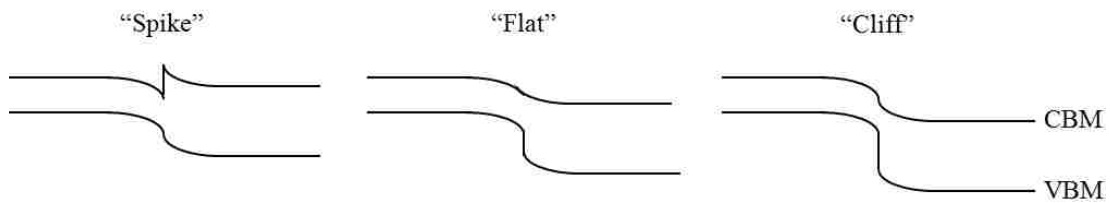
Figure 2.3: The three different possible heterojunction alignments: "spike," "flat," and "cliff."

2.2 Effects of CdCl$_2$-Treatment on CdTe Cells

It has long been understood that the presence of chlorine in CdTe films is a prerequisite for high efficiency solar cells.[11] A typical example for a post-deposition treatment or "activation" is CdCl$_2$ deposition on as-grown CdTe film, for example, by close space sublimation, followed by heating in air or vacuum and finally washing off the CdCl$_2$ residuals. Alternatively, CdCl$_2$ can be deposited on the heated CdTe film, therefore preventing residual formation. The structural and electronic effects of the chlorine treatment are rather similar – regardless of whether it is an *in situ* or post-deposition step. Basically all solar cell parameters (J$_{sc}$, V$_{oc}$, FF) improve with chlorine treatment.

Of the many effects of CdCl$_2$-treatment, CdTe/CdS interdiffusion is important for this work. Sulfur diffusion from the CdS to CdTe layer is enhanced.[12-13] Sulfur diffusion leads to the formation of CdTe$_{1-x}$S$_x$ by partial consumption of the CdS buffer layer. Thereby, the CdS thickness is reduced or, in the extreme case, completely consumed. Furthermore, Te is found to diffuse into the CdS layer.[14]

Increased conductivity or p-type doping shows up in a decreased series resistance of the device. This may be due to modified grain boundary potential as chlorine is mostly accommodated at the grain boundies.[15] Also, carrier lifetime typically increases from 200 ps to 2 ns[11] upon chlorine treatment. In accordance with such lifetime increase, an increase in diffusion length by a factor of 3 has been observed.

After CdCl$_2$ activation, the electronic levels have likely changed due to the above-mentioned effects. By mechanically cleaving a fully formed layer stack and by using many characterization techniques a complementary picture of the chemical interface structure of CdTe-based solar cells as a function of CdCl$_2$ treatment.

2.3 CdS and Alternatives

A major conversion loss in laboratory cells as well as commercial modules is due to adsorption of blue light in CdS layers.[2] The CdS layer strongly absorbs photons with energy greater than its bandgap of 2.4 eV. Electron hole pairs generated in the CdS layer do not contribute to the photocurrent, which is seen by a characteristic reduction of quantum efficiency for wavelengths $\lesssim$ 550 nm (2.25 eV).[16] It is therefore desirable to reduce the CdS layer thickness or to use other buffer layer materials with a larger band gap. When reducing the CdS layer thickness the probability of creating pinholes increases, which can lead to direct contact between the front contact (TCO) and the absorber layer (CdTe). The creation of these pinholes will create a poor p-n junction as seen by a reduced open circuit voltage, fill factor, and thus efficiency.

Latest record cells reported by General Electric and First solar exhibit significantly enhanced photocurrent densities and external quantum efficiencies >90% for wavelengths down to ~350 nm (3.54 eV).[17] Although the buffer layer composition is not reported, such properties are likely obtained using buffer layers with higher energy gaps. One way to obtain a similar band gap is alloying CdS with ZnS, which by controlling stoichiometry can have a bandgap of 2.42 – 3.66 eV[18]. Another method to produce a similar band gap is by alloying ZnO and MgO. This method has produced band gaps of 3.2 – 4.2 eV with low Mg content ($Mg_xZn_{(1-x)}O$, X $\leq$ 0.5).[19] A careful literature review shows this method has not been reported for CdTe-based devices and will be explored later in this work with emphasis on chemical and electronic properties at the interfaces.

Pervious record cells by Wu et al. have also shown high quantum efficiencies at low wavelengths (> 80% at ~425 nm or 2.91 eV)[8]. Similarly, Kephart et al. reported

quantum efficiencies > 75% for wavelengths ~400 nm (3.10 eV).[20] For both cases a sputtered oxygenated CdS layer was used. The chemical composition of such layers will be investigated and discussed below.

CHAPTER 3   EXPERIMENTAL METHODS

This chapter is designed to give a brief overview of the experimental methods used in this work and is not a complete explanation of all techniques used. Both lab-based and synchrotron-based Spectroscopies will be described as well as implemented microscopies. Also lesser-known analysis and sample preparation techniques will be explained.

3.1 Photoemission

The most common and powerful technique to study the chemical and electronic structure of surfaces and interfaces is Photoelectron Spectroscopy (PES). PES is based on the photoelectric effect, which was discovered in 1887 by Heinrich Hertz. The effect was later explained by Albert Einstein, which led to his Nobel Prize in 1921. In direct photoemission X-ray or ultraviolet photons interact with a sample surface. This interaction leads to the ejection of photoelectrons and provides information of the occupied density of states (DOS). Inverse photoemission spectroscopy (IPES) is, as the name implies, the inverse process to PES. In this case, a low energy electron impinges on the sample and relaxes to unoccupied states. This relaxation may be radiative, which contains information about the unoccupied DOS. By Combing UV PES (UPS) and IPES, the band gap at the surface can be directly determined.

3.1.1   Direct Photoemission

Photoelectron spectroscopy was the primary technique used to study the chemical and electronic structure. With this technique the occupied DOS is investigated by measuring the intensity of ejected photoelectrons as a function of the kinetic energy (E_{kin}) with respect to the Fermi energy (E_F) of the analyzer. The E_{kin} is then used to infer the

binding energy (E_{bin}) that the electron originated. The terms photoemission and photoelectron spectroscopy will be used interchangeable.

First the physical processes governing photoelectron spectroscopy will be discussed. Photoemission can be described as an electron moving from an initial state $|\Psi_i\rangle$ to a final state $\langle\Psi_f|$ by photon excitation. Using the dipole approximation the probability of this transition $w_{i\rightarrow f}$ can be described by Fermi's Golden rule:

$$w_{i\rightarrow f} \propto \left|\left\langle \Psi_f |\Omega| \Psi_i \right\rangle\right|^2 \delta\left(E_f - E_i - h\nu\right) \qquad (1)$$

conservation of energy is ensured by use of a delta function. The final state is a nonscattered electron with kinetic energy (E_{kin}). The initial state binding energy (E_{bin}) can then be calculated by the following equation:

$$E_{bin} = h\nu - E_{kin} \qquad (2)$$

Another important feature of Fermi's Golden rule is the transition probability that depends on both the initial and final state wave function of the electron. In other words, final state effect may not be negated. Figure 3.1 shows a schematic of both the X-ray and UV photoemission process.
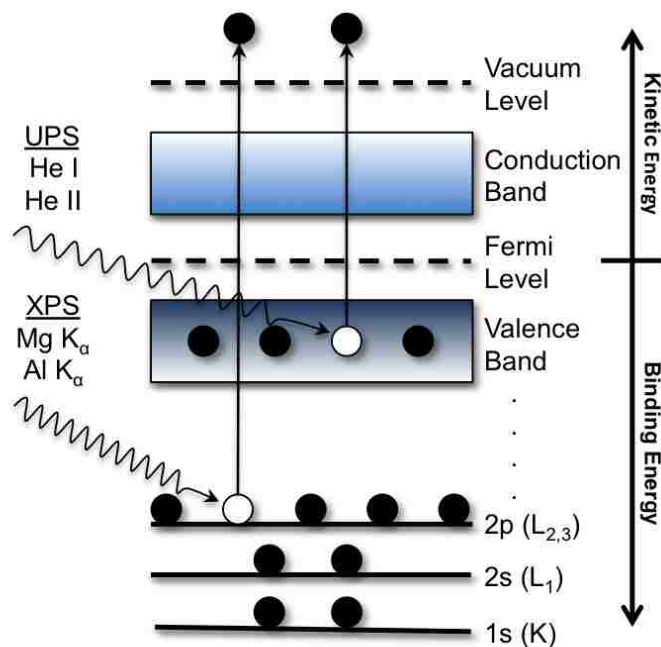
Figure 3.1: A Schematic representation of the photoemission process for XPS and UPS. The sample is irradiated with X-ray or UV photons that excite a photoelectron. The kinetic energy of the electron is measured.

X-ray Photoelectron Spectroscopy (XPS) is ideally suited to study the core electronic levels of a material. To perform XPS in a laboratory setting either a dual anode of which either Al $K_{\alpha 1,2}$ (1486.6 eV; 2p $\rightarrow$ 1s transition) or Mg $K_{\alpha 1,2}$ (1253.6 eV; 2p $\rightarrow$ 1s transition) radiation is used, or a monochromatic Al X-ray source is utilized. Ultraviolet Photoelectron Spectroscopy (UPS) is better suited for the study of shallow electronic levels and filled band states or the valence band (VB). Principally, these states could be studied with XPS, however the probability of photo-ionizing a valence band state is low. In this work either a He discharge lamp or He plasma generated with electron cyclotron resonance (monochromatic) is used. The He I (21.22 eV; 1s2p $\rightarrow$ 1s^2 transition) or He II (40.81 eV; 2p $\rightarrow$ 1s transition) excitations were utilized. PES is ideally suited for the study of surface states due to the energy dependence of the Inelastic

11

Mean Free Path (IMFP). The so-called "universal curve" (Fig. 3.2) shows the photoelectron energy dependence on the IMFP. Two lines are drawn to illustrate the approximate attenuation length for UPS and XPS.[21]
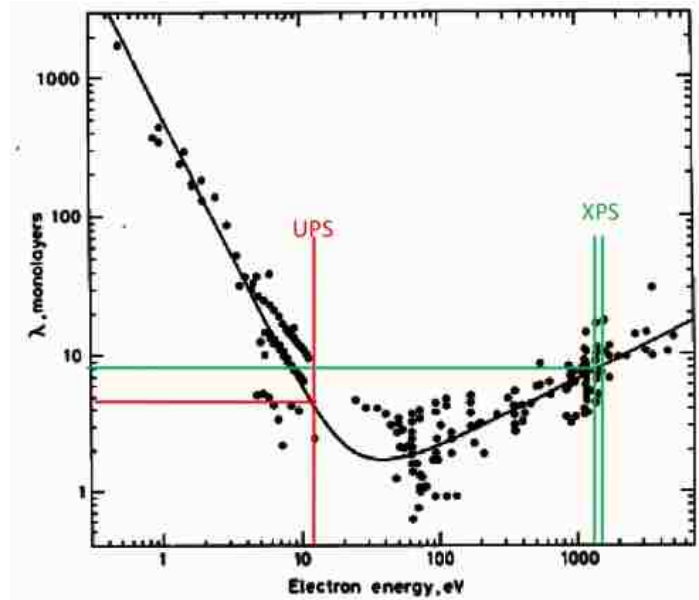
Figure 3.2: Inelastic mean free path of electrons as a function of their kinetic energy in various solids. Data points indicate measured values (adapted from Ref [21]).

PES experiments performed in the "Andere ESCA" machine utilized a SPECS PHOIBOS 150 MCD hemispherical analyzer and a dual anode X-ray source or a helium discharge lamp, respectively. Other PES spectra in this work were recorded using Scienta R4000 electron spectrometer in the "Scienta" system with a dual anode X-ray source, monochromatized Al K_α X-ray source, or Gammadata VUV 5000 microwave-excited monochromatized UV source. The energy scale of the electron analyzers for XPS measurements were calibrated according to Seah [22] using the photoemission lines of clean Au, Ag, and Cu. The energy scale for UPS was calibrated to the Fermi energy of a clean Au foil. PES spectra were recorded in fixed analyzer transmission mode where the pass energy remains fixed for the collection of a spectrum.

Such experiments are performed in vacuum due to three main reasons: (i) the surface composition of the sample must not change during the experiment, (ii) the photoelectrons ejected from the sample must travel thought the analyzer without colliding with other particles, and (iii) some experimental components requires the need for ultra-high vacuum (UHV; P<10^{-9} mbar) as opposed to high vacuum (10^{-4} – 10^{-9} mbar). In the kinetic theory of gases, the ratio of adsorbed particles to the number of free particles at various pressures can be determined. At a pressure of 10^{-6} and 10^{-11} mbar, the ratio of absorbed particles to the number of free particles is 10^{4} and 10^{9}, respectively. The mean free path λ (i.e., average path each particle travels between collisions) is inversely proportional to the number density of molecules present where the latter is directly proportional to the gas pressure.

3.1.2   Inverse Photoemission

Inverse photoemission spectroscopy (IPES) is the inverse process of PES. Here, electrons are impinged onto the surface of a sample and the incident electrons decay into unoccupied electronic states and emit photons. This process is shown schematically in Fig. 3.3. From this technique, the spectrum of *unoccupied* DOS is obtained and the conduction band minimum (CBM) can be determined. The electron source is a low energy electron gun using thermionic emission from a filament (STAIB). The energy of the electron gun is varied (E_{kin}: 6 – 16 eV), and when an electron relaxes into an unoccupied state in the conduction band, a photon is emitted. The detector used for the IPES experiments is similar to a Geiger-Müller counter. The detector consists of a SrF_2 entrance window to a tube with $Ar:I_2$ filling and high-voltage rod. The window and I_2 filling serves as the high and low energy detection limits, respectively. The SrF_2 window

does not transmit radiation with energy greater than 9.8 eV.[23] While the lower detection limit is determined by the threshold for the molecular photoionization of iodine,

$$I_2 + hv \rightarrow I_2^- + e^-$$
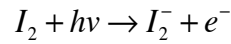
at 9.37 eV.[24] Thus, the photons are detected in isochromat-mode as a function of electron energy. However, the ratio of cross section of IPES to UPS is about 10^{-5} which makes it a more difficult and time consuming experiment.[25] Energy calibration was performed by measuring the Fermi level of a clean Au foil, and all subsequent spectra are referenced to the Fermi level. The IPES experiments were also performed in the analysis chamber of the Andere ESCA. The experimental resolution, as determined by the Fermi fit of the clean Au foil, for this particular IPES set-up can be as low as 0.3 eV.
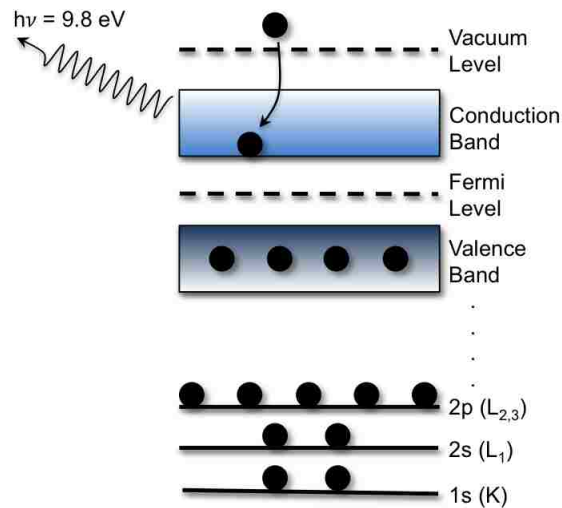
Figure 3.3: A schematic energy diagram of the IPES process. An electron source impinges electrons (of varying E_{kin}) to the surface of a sample, where the electron relaxes into a lower unoccupied state and emits a photon.

3.1.3   Combining UPS and IPES

The surface band gap (E_g) of a material is experimentally determined by combining information about the VBM (by UPS) and CBM (by IPES). Both of these techniques are very surface-sensitive since the information depths are 2 - 4 nm based on the approximate IMFP shown in Fig. 3.2.[26] The band edges (VBM and CBM) are determined by linear extrapolation that intersects the baseline. At this intersection, a state may not necessarily exist at that energy level, but this is the best approximation for the uppermost state (for the valence band). Other arguments for the linear extrapolation method include non-symmetric broadening towards higher E_B from: downward dispersion of the VBM in all directions in reciprocal space, the inelastic scattering process (*e.g.*, photons and electrons), and the possibility of incomplete screening of a core hole.[27] The linear extrapolation procedures are justified experimentally for determining the E_g.[28] The electronic surface E_g may be different from bulk E_g measurements since the surface composition of a material could differ from the bulk phase. However, the surface electronic properties of materials are key pieces of information for successfully incorporating other materials into devices (*e.g.*, their interfaces). The energies of the VBM and CBM are essential pieces to understand the electronic properties of a material, and are required for deeper insight into device physics.

3.1.4   X-ray Excited Auger Electron Spectroscopy

While undergoing XPS experiments, X-ray excited Auger electron spectroscopy (XAES) is also performed. When a core hole is created by X-ray photons, one mechanism for the relaxation of the core hole is the Auger process. In the Auger process, an electron from an outer energy level (*i.e.*, of less binding energy) relaxes into the core

15

hole. An energy difference arises due to that transition, and the energy can either be absorbed by another electron and as a result be ejected or emitted as a photon. The first process is the Auger emission, while the second process is X-ray fluorescence (or emission; see 3.2.1) The XAES process is shown schematically in Fig. 3.4 for an oxygen atom. The ejected Auger electron is also detected by the electron analyzer. The notation for an XAES transition includes information from all three electrons involved, and follows traditional X-ray spectroscopic notation. For example, the O $KL_{2,3}L_{2,3}$ XAES line consists of the core hole created in the 1s level (i.e., K), an electron that relaxes to that core hole from the 2p level (i.e., $L_{2,3}$), and the detected electron (also) from the 2p. In general, XAES line shapes can be very indicative of the chemical environment since the electron emitted (associated with the XAES spectrum) are typically valence electrons.
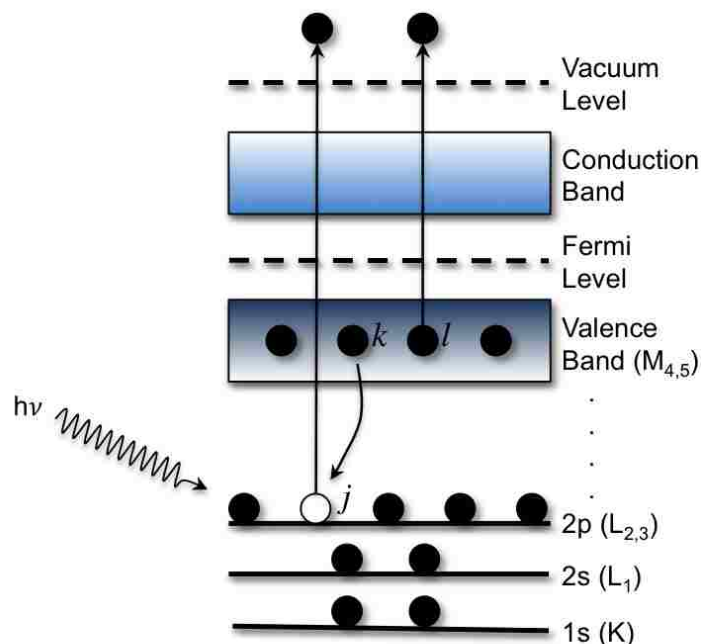
Figure 3.4: A Schematic representation of the photoemission process for XPS and UPS. The sample is irradiated with x-ray photons that excite a photoelectron from the $L_{2,3}$ state. An outer shell electron relaxes from the $M_{4,5}$ state into the core-hole. Energy is transferred to a third electron which is emitted from the $M_{4,5}$ state. This is recognized as a $L_{2,3}M_{4,5}M_{4,5}$ Auger emission.

3.1.5 Curve Fitting

During the course of this work analysis could not effectively be accomplished by only qualitative spectral analysis, for these cases curve fitting may be used. A general-purpose peak fitting program, Fityk, was utilized.[29] To describe a photoelectron spectrum at least two functions where used.

First a function, which approximates background, was added. The background of an XPS spectrum is dominated by scattered photoelectrons. The scattering of a valence electron into the conduction band is of most interest. In general the final energy of a

17

photoelectron can be described as the initial energy (eq. 2) minus some scattering energy. For metals the scattering energy can be infinitely small, resulting in a "step" of the background. This "step" can be described by a Shirley function.[30] In the case of a semiconductor, the minimum scattering energy is equal to the band gap; therefore the first scattered electrons will be shifted to lower kinetic energies by the band gap. The shape of the resulting feature is a small inflection point, because the scattering probability is rather low never the band gap due to low density of states at the band edges. For small energy windows, the background can be described as linear.

The remaining functions are used to describe the photoelectron peaks. Again, metals and semiconductors cannot be treated the same. For semiconductors, a Voigt function is used, which has both Gaussian and Lorentzian character. Lorentzian broadening is used to describe lifetime broadening effects of the core-hole, while Gaussian broadening nicely describes experimental broadening. Because electrons in a metal can have an infinitesimally small energy loss the photoelectric peak is not symmetric. There is a tail on the low kinetic energy side of the peak. This shape is best described by a Doniach-Sunjic function.[31]

3.2 Synchrotron-based X-ray Spectroscopy

In some cases, the light source needs to be highly brilliant and/or tuneable. For these cases experiments were performed at the Advanced Light Source, Lawrence Berkeley National Laboratory at Beamline 8.0.1. Synchrotron radiation, for the purposes of this work, was produced by passing electrons at near-relativistic speed through an undulator. A series of alternating magnets send the electrons in an undulating path, which produces near-monochromatic electromagnetic radiation. The distance between magnets

is varied to change the photon energy. For an undulator with N periods, the brightness (photons/sec/mm^2/mrad^2/0.1% BW) can be up to N^2 more than a single magnet, due to constructive interference. The brightness of an undulator is approximately 10 orders of magnitude greater than a lab-based X-ray source.

3.2.1   X-ray Emission Spectroscopy

As mentioned in the previous sections, photons are used to eject a core electron, thus leaving "behind" a cole hole. The core hole can be relaxed by either the non-radiant Auger decay (see section 3.1.4) or radiant fluorescence (*i.e.*, X-ray emission) process. As seen in Fig. 3.6, the Auger decay process dominates for lighter elements (atomic number < 20) for K-shell (*i.e.*, n=1) core holes.[32]
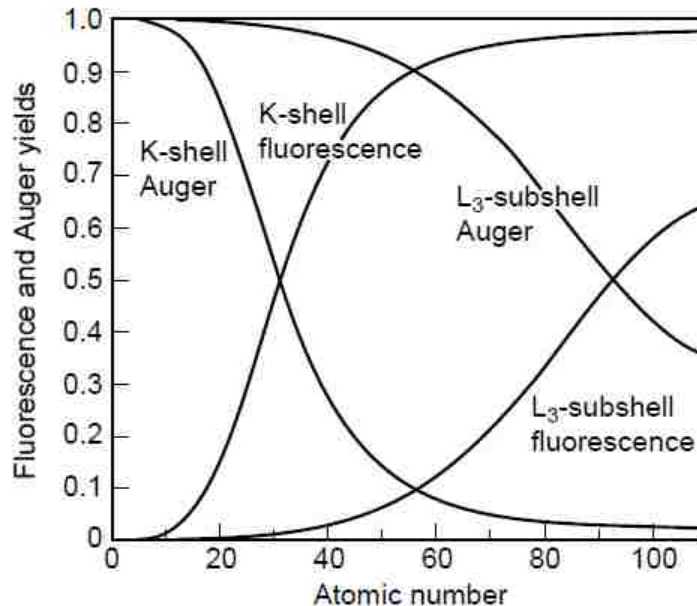
Figure 3.5: The yields for competing fluorescence and Auger relaxation processes for a photoexcited core hole.[32]

However, due to the much greater flux of photons at a synchrotron and the design of high-efficiency spectrometers, experiments utilizing the fluorescence decay are now

on a comparable measurement time-scale to that of laboratory-based spectroscopic techniques. In the fluorescence process, the core hole is filled by an electron from a higher energy level (*i.e.*, either a valence or core-electron), and the energy difference from this transition is emitted as a photon. This process is illustrated in Fig. 3.6.
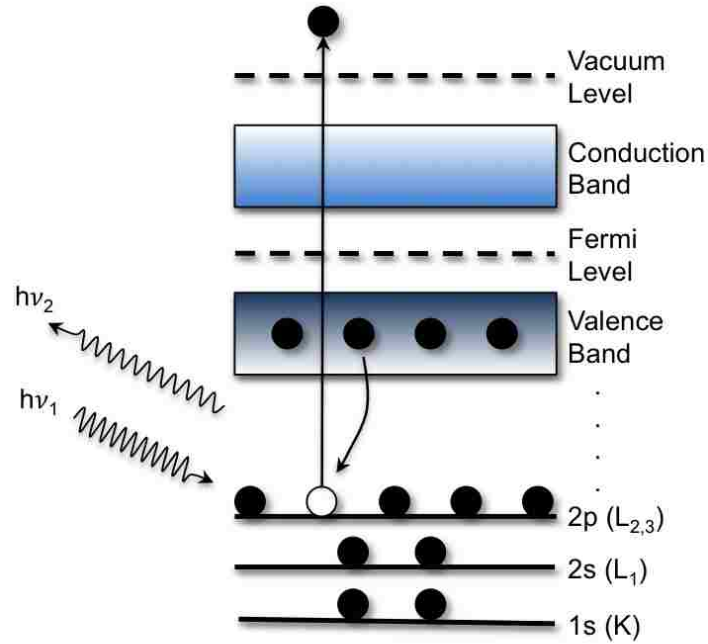
Figure 3.6: A schematic energy diagram of the X-ray emission process.

The X-ray emission process obeys the dipole selection rule, $\Delta\ell = \pm 1$, where ℓ is the azimuthal (or angular momentum) quantum number. The intensity of the emitted photons in XES also follows Fermi's golden rule as,

$$P\left(\psi_f \psi_i\right) \propto \left|\left\langle\psi_f\left|\hat{H}\right|\psi_i\right\rangle\right|^2 \delta\left(h\nu - \left(E_i - E_f\right)\right).$$

In addition, the intensity of the XES signal is also dependent on the exponentially attenuated intensity of the incoming photon and outgoing photon. X-ray attenuation lengths through many types of materials are tabulated.[33] XES experiments can be tuned

(by selecting a suitable photon energy) to a specific "edge" of an element (*i.e.*, energy level) such as the K-edge (1s). Like PES, XES probes the occupied density of states of a particular element. This technique paints an element-specific partial density of states electronic picture, while XPS, UPS, and IPES portrays the *total* density of states.

XES experiments were performed on Beamline 8.0.1 at the Advanced Light Source (ALS), Lawrence Berkeley National Laboratory. At Beamline 8.0.1, the synchrotron radiation exits an undulator, then passes through the barn doors, the first vertical focusing mirror, the entrance slit, monochromator spherical grating, the exit slit, and finally a re-focusing mirror to direct the beam. The set up (including optical elements) used in Beamline 8.0.1 is shown in Fig. 3.7. The experiments were performed in either the permanently installed Soft X-ray Fluorescence ("SXF") endstation[34] or the Solid and Liquid Spectroscopic Analysis ("SALSA") endstation.[35] The SXF spectrometer has a spectral resolution $E/\Delta E$ between $400 - 1900$. In SALSA, the high-efficiency variable line spacing (VLS) spectrometer was used, and has a spectral resolution of $E/\Delta E$ > 1200 over the whole energy range ($80 - 650$ eV).[35]
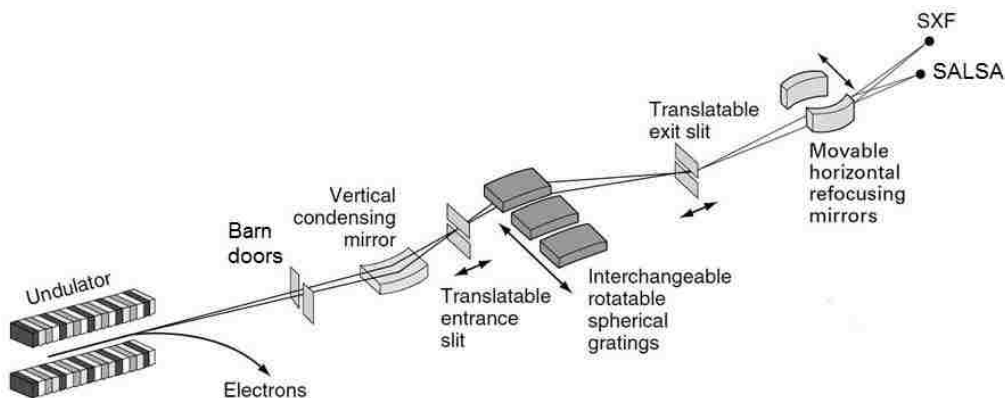
Figure 3.7: A schematic layout of the synchrotron radiation path in Beamline 8.0.1 at the ALS.

3.3 Microscopy

During the study of surface chemical and electronic properties, an understanding the surface morphology may be critical to interpreting data.

3.3.1   Atomic Force Microscopy

During the course of this work atomic force microscopy (AFM) was the primary morphological tool used. AFM is primarily performed in either contact or non-contact modes. In contact AFM (C-AFM) a cantilever with a sharp tip is rastered over surface. When the tip is brought close to the surface, forces between the tip and the sample deflect the cantilever in accordance with Hooke's law. During scanning a feedback mechanism is employed to adjust the tip-to-sample distance, which maintains constant force (deflection) between tip and sample. When non-contact AFM is employed the cantilever tip does not contact the surface rather, the cantilever is oscillated at some frequency. The van-der-Waals forces, which are strongest from 1 nm to 10 nm above the surface, damp the monitored frequency. This dampening in concert with a feedback loop keeps the tip a constant distance from the sample. By monitoring the deflection or tip height adjustments a three-dimensional surface profile is provided. However, AFM does not provide any chemical information.

3.3.2   Scanning Electron Microscopy / Energy Dispersive X-ray Spectroscopy

To gain both chemical and morphological information scanning electron microscopy was used during this work. Here a focused beam of high-energy electrons (2-

20 keV) is scanned over a surface. Interacts of the electron beam with the sample is typically measured by back-scattered (BSE) or secondary (SE) electrons. The intensity of BSE or SE signal as a function of beam position to produce an image. The ratio of BSE/SE is a function of atomic number and beam energy. The combination of both signals can be used to interpret relative atomic mass for various features/locations.

3.4 Sample Preparation

3.4.1 Ion Treatment

Occasionally samples must be produced in or exposed to air. The resulting film will have an adsorbate layer, which will make determining the surface band alignment difficult, if not impossible. Ion stimulated desorption has be developed to remove surface contamination while minimizing damage to the surface. Here, a low energy ion beam, normally 50 eV Ar^+, is directed towards the surface and transfers enough energy to release any adsorbed gases into the vacuum chamber. During this work ions where also used to sputter away surface. In this case higher energy ions, 100 - 5000 eV, strike the sample surface with enough energy to break most bonds. By removing the uppermost layer chemical properties can be investigated of the sub-surface, however some information about the electronic properties (e.g., band edges) have been lost.

3.4.2 Temperature Stressed Cleaving

Interfacial chemical and electronic properties are needed to effectively optimize device performance. Normally these properties are investigated during stepwise growth or sputter depth profiling, however these are not very effective for CdS interfaces because

of diffusion (see 2.2). A cleaving approach was employed to gather information about a buried interface with minimal damage to the electronic properties.

Metal sheets are attached to both sides of a sample (i.e., glass and absorber) with a vacuum safe conductive silver epoxy. The epoxy is cured on a hotplate overnight to ensure a strong bond with the metal sheet. Traditionally, force is applied to separate the layer stack, however in the case of CSU grown films separate within the adhesive layer (i.e. epoxy found on both sides of the cleave). This suggests strong adhesion of the layers within the device. For the purposes of this work temperature stressed cleaving was conducted. Once the epoxy has cured the sample is submerged in liquid nitrogen. It is believed that the interface with the largest mismatch coefficient of thermal expansion can be strained to the point of delamination.

CHAPTER 4   LOW ENERGY ION TREATMENT OF CdCl$_2$-TREATED CdTe

SURFACE

The following chapter is previously published in Photovoltaic Specialists Conference Proceedings and reports work performed to study the chemical and electronic properties of CdTe surfaces. © 2012 IEEE. Reprinted, with permission, from D. Hanks, M. Weir, K. Horsley, T. Hofmann, L. Weinhardt, M. Bär, K. Barricklow, P. Kobyakov, W. Sampath, C. Heske, Photoemission study of CdTe surface after low-energy ion treatments, Photovoltaic Specialists Conference (PVSC), 2012 38th IEEE, June 2012.

4.1 Introduction

While Si-based devices currently dominate photovoltaic energy production, thin-film devices based on CdTe offer are possible candidates for cost-efficient alternatives with high conversion efficiency[1]. To further improve CdTe-based devices, a deeper understanding of the electronic transport, in particular through the various interfaces of the device, is of significant interest. Surface-sensitive photoelectron spectroscopy is an ideal tool to study the electronic and chemical properties of surfaces and interfaces, including interfacial band gaps and band offsets in the valence and conduction band. However, before such surface-sensitive methods can be employed, surface adsorbates or oxides, which can significantly impact the results, need to be removed. This contribution therefore studies the impact of a low-energy ion surface treatment on the electronic and chemical surface properties of an air-exposed CdTe thin film, monitoring the effectiveness and suitability of such surface cleaning for the preparation of relevant CdTe thin-film surfaces and interfaces.

4.2 Experimental Details

The $CdCl_2/CdTe/CdS/SnO:F/SiO_2$ layer stack was grown at CSU using heated pocket deposition (HPD), a modified close-spaced-sublimation (CSS) method in an in-line continuous vacuum system[36]. The sample was placed in front of a CSS pocket for a time commensurate with the desired layer thickness, after which it was moved to the next CSS pocket[36]. $CdCl_2$ treatment was performed by vapor deposition using the CSS method, after which samples were rinsed first with deionized water and subsequently with isopropyl alcohol and then dried for ~10 s in 100 °C air. After production, samples were vacuum-sealed (to avoid further surface contamination) and shipped to UNLV for characterization. The samples were unpacked in the inert environment of a dry nitrogen-filled glovebox and directly introduced into the ultra-high vacuum (UHV) system with a base pressure below 5×10^{-10} Torr.

X-ray photoelectron spectroscopy (XPS) was performed using a monochromatized Al K_α x-ray source (VG Scienta MX650) and a VG Scienta R4000 electron analyzer, calibrating the energy scale according to ISO 15472[22]. For UV photoelectron spectroscopy (UPS), a monochromatized UV source (VG Scienta VUV5000 with VG Scienta VUV5040 Monochromator) and He II_α radiation was employed. The energy scale of UPS was calibrated to that of the Fermi energy of a clean gold foil reference. The ion treatments were performed using a Thermo Scientific EX05F ion gun with Ar^+ ions at energies of 100 and 200 eV, with a sample current of 0.2 and 0.7 µA, respectively.

4.3 Results and Discussion

4.3.1 Chemical composition

Figure 4.1 shows an XPS survey spectrum of the as-received CdTe surface (a), after a first ion treatment at 100 eV (b), and after several treatments at 100 and 200 eV (c). For the as-received sample, we find the expected photoemission and Auger lines of Cd and Te, and in addition C- and O-related signals due to surface adsorbates and surface oxidation caused by air exposure. The absence of a Cl 2p peak (at 199 eV) suggests that no Cl is present at the surface. However, corresponding X-ray Emission Spectroscopy (XES) measurements (not shown), which are more bulk-sensitive compared to the XPS data shown here, clearly indicate the presence of Cl in the sample.
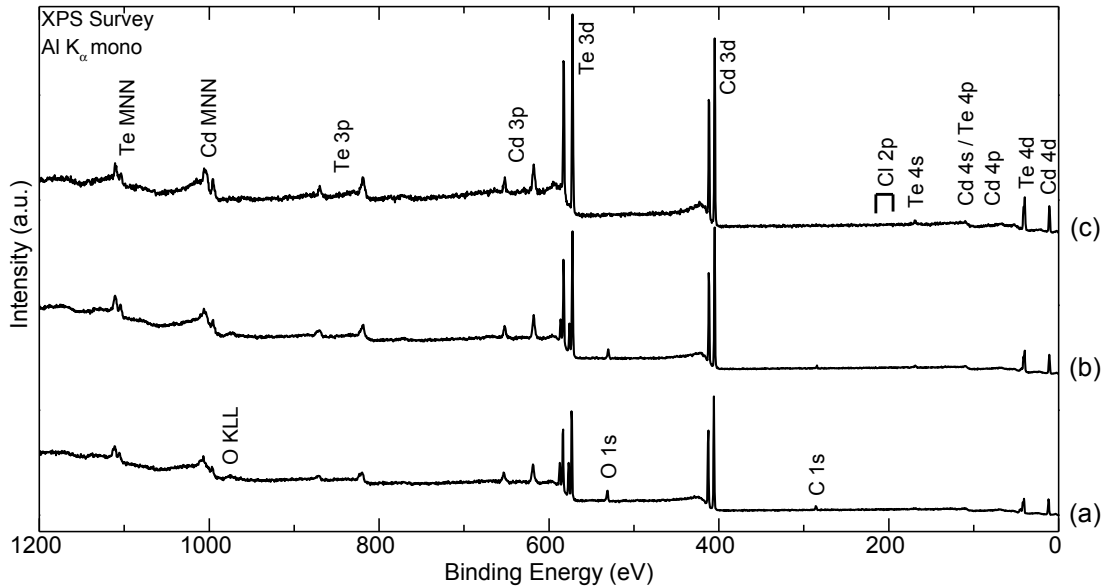
Figure 4.1: XPS survey spectrum of the CdCl$_2$-treated CdTe thin-film surface prior to ion treatment (a), indicated the presence of Cd and Te (as expected), as well as C and O in the surface. The same sample after the first100 eV ion treatment step (b) shows a decrease in the O and C signals, along with an increase in Te and Cd intensity. The CdTe sample after the last (200 eV) ion treatment step (c) displays no O or C signal and further increase Te and Cd signal.

In order to measure the electronic surface structure of the CdCl$_2$-treated CdTe without influence of surface contaminants, low-energy ion treatment was employed. After each Ar$^+$ ion cleaning step (100 or 200 eV for 15 min), the chemical and electronic structure of the sample was measured with XPS and UPS.

The first cleaning step with 100 eV Ar$^+$ ions resulted in a significant decrease of the O and C signal and an increase in the Cd and Te signals, as can be seen in Figure 4.1 (b). Furthermore, Te 3d$_{5/2}$ detail spectra in Figure 4.2 (left panel), normalized to the background at lower binding energy, reveal a strong reduction of the peak indicative for Te-O bonds at 576 eV and a 0.2 eV shift of all peaks to lower binding energies. This shift is likely due to a change of the band bending towards the surface after removal of the uppermost surface adsorbates.[37] With further treatment time, only the Te 3d$_{5/2}$ peak shifts slightly further to lower binding energies (by 0.05 eV) and broadens (by 0.7 eV).

XPS
Al K$_\alpha$ mono

Te 3d$_{5/2}$

O 1s

C 1s

Te-O

CdTe

Normalized Intensity (a.u.)

100eV

0 min

15 min

30 min

45 min

60 min

3 Week UHV

200 eV

15 min

30 min

45 min

60 min

578   574   570   534   531   528   289   285   281

Binding Energy (eV)
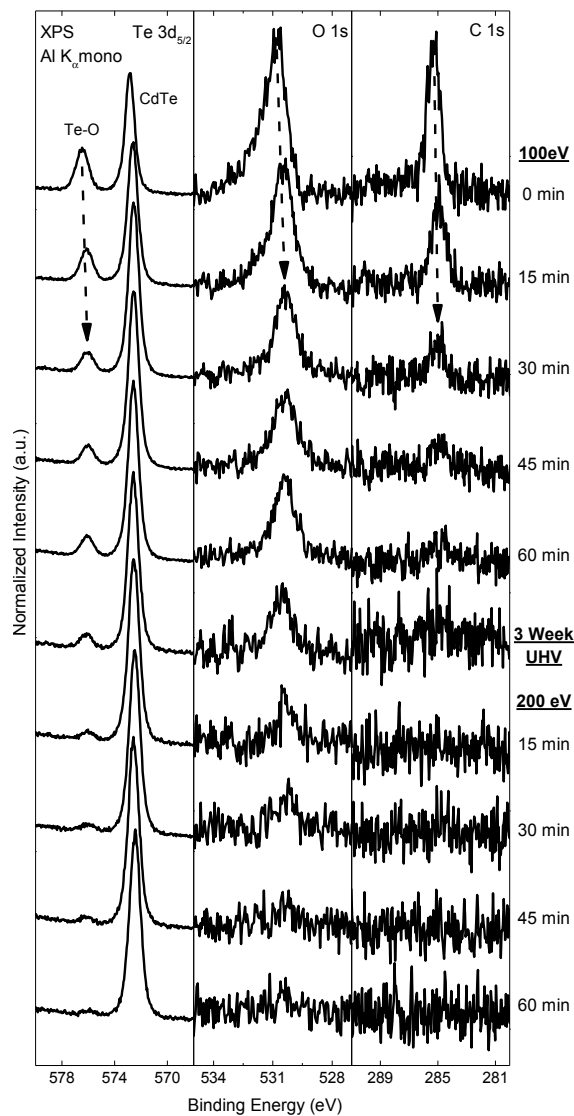
Figure 4.2: XPS detail spectra of Te 3d$_{5/2}$ (left), O 1s (center), and C 1s (right) after each ion treatment step.

However, no asymmetry of the peak can be found, which would point towards the development of a second, chemically different Te species (e.g., metallic Te) outside the range of published binding energies for CdTe[21, 38-39]. In contrast, we attribute the broadening to the surface being roughened by impact with Ar$^+$ ions, leading to a less well-defined chemical environment for the Te atoms. A similar behavior can be found for

29

the Cd 3d peak, again giving no indication for the formation of an elemental Cd component.

To characterize the surface stoichiometry, the Te $3d_{5/2}$ and Cd $3d_{5/2}$ peak areas were determined by a fit of the detail spectra. The derived intensities were corrected by the respective photoionization cross-sections[40], the transmission function of the analyzer, and the attenuation length of the emitted electrons[41]. Figure 4.3 shows the relative amounts of Cd, Te, Te-O, and (Te + Te-O) as a function of surface cleaning steps. While the absolute error bars of these values are rather high, the relative uncertainty between the values at different treatment times is much smaller. As mentioned above, we find a strong decrease of Te in a Te-O bonding environment in particular for the first treatment steps. Furthermore, the relative amount of Te seems to increase slightly, while that of Cd decreases until both reach the expected 1:1 stoichiometry (after a cleaning time of 60 min). This apparent change in surface stoichiometry can be attributed to differences in the inelastic mean free paths associated with the Cd 3d and Te 3d lines, 2.3 nm and 2.6 nm[41], respectively. For no or short cleaning times, the shorter attenuation length of the Te 3d lines leads to stronger attenuation in the adsorbate layer (compared to the Cd 3d lines). In contrast, after prolonged ion treatment, adsorbates are removed and hence the stoichiometry of the underlying CdTe "surface" can be observed.
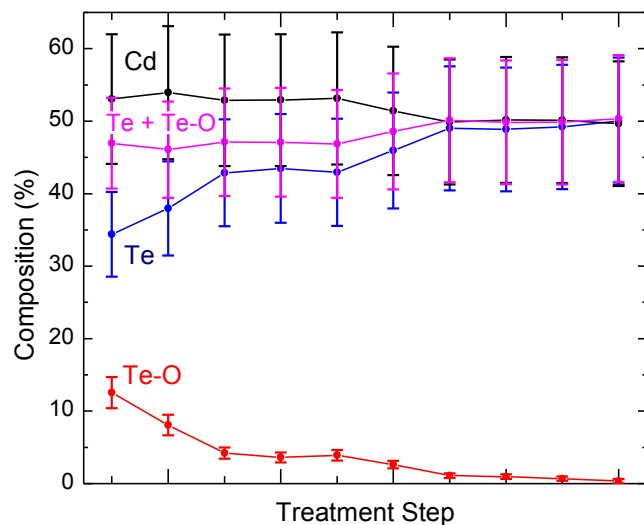
Figure 4.3: Surface composition as derived from XPS as a function of ion treatment time.

After 45 min of 100 eV ion treatment, the C signal becomes indistinguishable from the noise level, while the Te-O contribution to the Te $3d_{5/2}$ and O signals can still be clearly identified (see Figure 4.2). This shows that the ion treatment was not completely effective in removing all oxidized species from the surface. The sample was then stored in UHV for 3 weeks. After this time, a slight decrease of the O 1s and the Te-O signals as compared to the last measurement before storage can be observed. This is speculatively attributed to a slow desorption of O-containing species (e.g., water molecules). To further remove oxides from the surface, ion treatments using ion energies of 200 eV were then employed.

Much like the 100 eV treatment, the first 15 min step at 200 eV resulted in a significant decrease of the Te-O and O signal, and thereafter some additional but slower decrease of these signals was observed. Again, the Te and Cd peaks broaden slightly with treatment time, presumably due to surface roughening. After 45 min of 200 eV ion treatment, the O 1s signal was reduced to within the noise level of the measurement, and

at 60 min the Te-O component of the Te $3d_{5/2}$ peak (which has a six times higher cross-section than O $1s^{40}$) nearly vanished as well. At no time during the 200 eV treatments did the C 1s signal reappear. This shows that the C and O signals observed prior to cleaning were only localized at the surface and not built into the CdTe layer.

4.3.2   Electronic properties

During the 200 eV ion treatment series, UPS was utilized to also monitor the position of the VBM with respect to the Fermi energy (Figure 4.4). The VBM shifts towards the Fermi energy during the first 15 min of cleaning with 200 eV ions, but then remains constant within the error of the linear extrapolations used to determine the band edge position. After 60 min of 200 eV ion treatment, the VBM is found (0.8 ± 0.1) eV below the Fermi level.
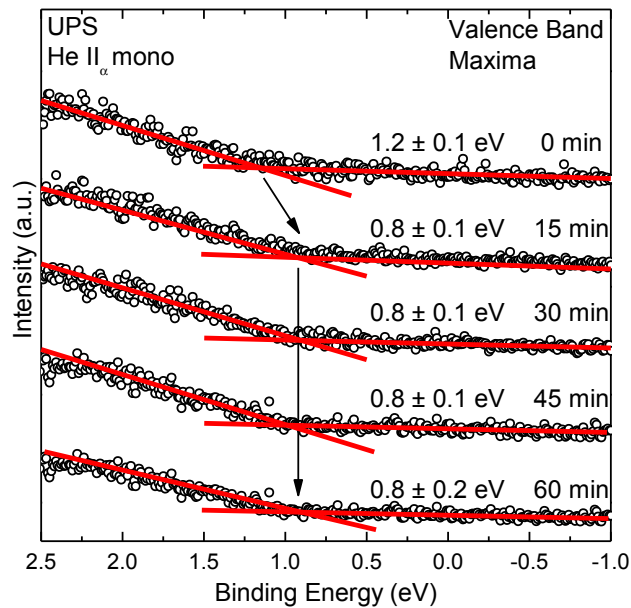
Figure 4.4: UPS measurement and linear extrapolation of the valence band maximum as a function of 200 eV Ar$^+$ ion treatment time. The binding energy is given with respect of the Fermi energy.

This value represents the lower "half" of the band gap, which is expected to be close to the bulk band gap of 1.5 eV[42], and thus suggests an approximately mid-gap position of the Fermi energy. However, widening of the band gap towards the surface has been shown in other photovoltaic thin film absorbers (Bar, et al. [43] and references therein) and cannot be ruled out at this point. In fact, the presence of a "wide-gap" material between the CdTe absorber and the back contact, especially when introducing an upward shift of the conduction band, could potentially reduce electron-hole recombination at the back contact interface.
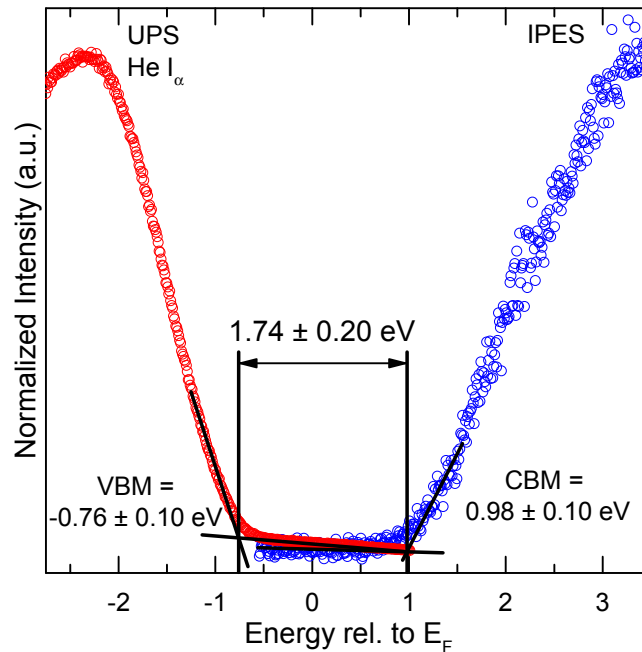
Figure 4.5: Combined UPS and IPES spectra of the cleaned CdCl$_2$-trated surface after low-energy ion cleaning and storage in vacuum for one week. A VBM and CBM of -0.76 and 0.98 ± 0.10 eV are found.

To evaluate these two interpretations of the valence band maximum IPES was conducted. The sample was stored in ultra high vacuum for ~ 1 week until the sample could be measured. The sample was first checked for changes with XPS (not shown),

which none could be found. UPS and IPES measurements (Figure 4.5) show a VBM of -0.76 ± 0.10 eV that is in agreement with measurements prior to UHV storage. The lack of a change further suggests the sample is electronically identical to ~ 1 week prior. A similar evaluation of the IPES data gives a CBM of 0.98 ± 0.10 eV. By combining the information gathered from the valence band and conduction band measurements, a surface band gap of 1.74 ± 0.20 eV is seen, which is slightly larger than the 1.5 eV bulk band gap[42].

4.4 Summary

We have investigated the possibility of removing surface oxides and adsorbates with low energy Ar^+ ion treatment steps. Surface-sensitive XPS data show the removal of oxygen and carbon with increased treatment times and energy. Careful monitoring of the chemical and electronic surface structure of the treated CdTe surface shows no indications for preferential removal of Cd or Te. However, the broadening of core-level spectra points to a treatment-induced roughening of the CdTe surface. Measurements of the surface band gap show an upward shift of the conduction band and a "wider-gap" material between the CdTe absorber and the back contact, which could potentially reduce electron-hole recombination at the back contact interface.

CHAPTER 5   EFFECTS OF $CdCl_2$ ON THE CdS/SnO_2 INTERFACE

5.1 Introduction

CdTe/CdS-based thin-film solar cells are established candidates for cost-effective devices yielding high efficiencies[1]. To further improve their performance, a fundamental understanding of the chemical and electronic interface structure throughout the $CdCl_2$-treated $CdTe/CdS/SnO_2$:F/glass layer stack is necessary. Significant diffusion processes occur during manufacturing, particularly induced by the post-deposition $CdCl_2$-treatment. Thus, most interfaces in the device are not fully formed until after these treatments, presenting a challenge to standard surface-science characterization approaches of step-wise material deposition. Sputter depth-profiling techniques have been used to investigate the effects of $CdCl_2$, but these techniques are destructive and suffer from a variety of shortcomings, including preferential sputtering, sputter-induced mixing, and matrix effects.

5.2 Experimental Details

The $CdCl_2/CdTe/CdS/SnO_2$:F/SiO_2 layer stack was grown at CSU using heated pocket deposition (HPD), a modified close-spaced-sublimation (CSS) method in an in-line continuous vacuum system[36]. The sample was placed in front of a CSS pocket for a time commensurate with the desired layer thickness, after which it was moved to the next CSS pocket[36]. $CdCl_2$ treatment was performed by vapor deposition using the CSS method, after which samples were rinsed first with deionized water and subsequently with isopropyl alcohol and then dried for ~10 s in 100 °C air. After production, samples were vacuum-sealed (to avoid further surface contamination) and shipped to UNLV for characterization.

The samples were unpacked in the inert environment of a dry nitrogen-filled glovebox and prepared for cleaving. A small amount of fast setting conductive silver epoxy was applied to the glass and CdTe surface followed by stainless steel sheet. The sample was then allowed to cure on a hot plate at 60 °C overnight (~16 hr) while still in the glovebox. The sample was then removed from the hot plate and, while warm, submerged in LN_2. The layer stack cleaved with minimal to no force and directly introduced into the ultra-high vacuum (UHV) system with a base pressure below 5×10^{-10} Torr.

5.3 Results and Discussion

5.3.1 Determination of the cleaving location

XPS survey of the four cleaved surfaces (two interfaces) are shown in figure 5.1. Samples from the CdTe side of the interface are notated as "Liftoff side" while the opposite is called "Glass side." Samples that were treated with $CdCl_2$ are denoted as red lines and without treatment are black lines. The Liftoff side of both samples peak associated to Cd, S, O, C, Sn, and Te are found, however by analyzing peak intensities we can say the surface of the liftoff side to predominately be Cd and S. Cl is also found on the liftoff side and can be categorized as a predominate peak. Evaluating the glass side in a similar fashion, the surface is predominately Sn and O with small contributions of Te, Cd, C, S, and Cl. The relative abundances of the various elements suggest the cleaving plane to be at/near the CdS/SnO_2 interface.
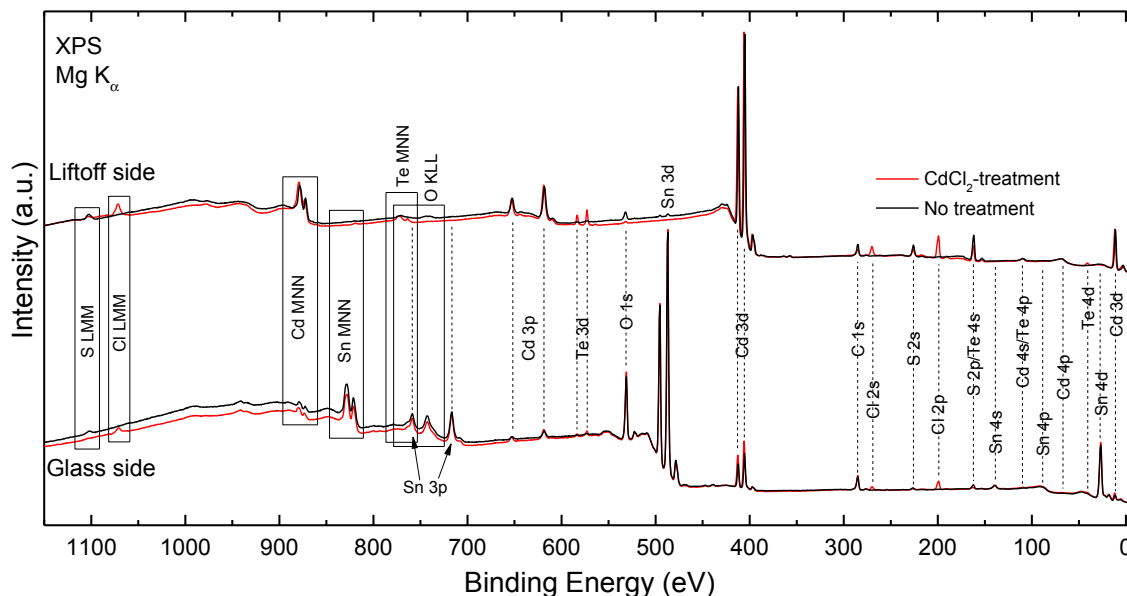
Figure 5.1: Mg K_α-excited survey spectra of the Liftoff (upper) and Glass (lower) sides of the cleaving interface of a CdCl$_2$-treated (red) and non-treated (black) CdTe layer stack.

The presence of C is likely due to either residual material left from the glass cleaning process or the low vacuum (40 mTorr) environment that the samples were produced in. Te is also found of the surface of the liftoff side; again two theories can explain the effect. The first begin a tearing of the interface, which results in holes in the liftoff side and islands on the glass side that terminate in CdTe. The second theory, the CdS/CdTe interface is diffused to such a large degree that Te is found throughout the CdS film. This may not be unusual, Dhere, et al. [44] has shown a significant increase in interdiffusion due CdCl$_2$-treatment. Furthermore, S is found to diffuse all the way to the surface of the CdTe film.[45]

5.3.2 Cleaving morphology

To investigate the cleaving morphology of the interfaces AFM images were collected on the two surfaces. By collecting images from multiple regions, there are two

37

distinct morphologies (Figure 5.2). The majority of the surface is flat and smooth. Surface measurements in this region would only be probing the CdS or SnO_2 layer respectively. When measuring closer to the edges of the sample (1-2 mm) a tearing can be found. ~100 nm deep holes are seen on the liftoff side of the interface and comparable islands on the glass side. Surface measurements in this area would be a sum of information from the CdS or SnO_2 surface and the holes or islands, respectively. Given measurement parameters of the spectrometer the expected measurement spot size is 5 mm in diameter.[46] Therefore, we can assume the spectroscopic information to be only from the smooth flat regions of the sample surface.
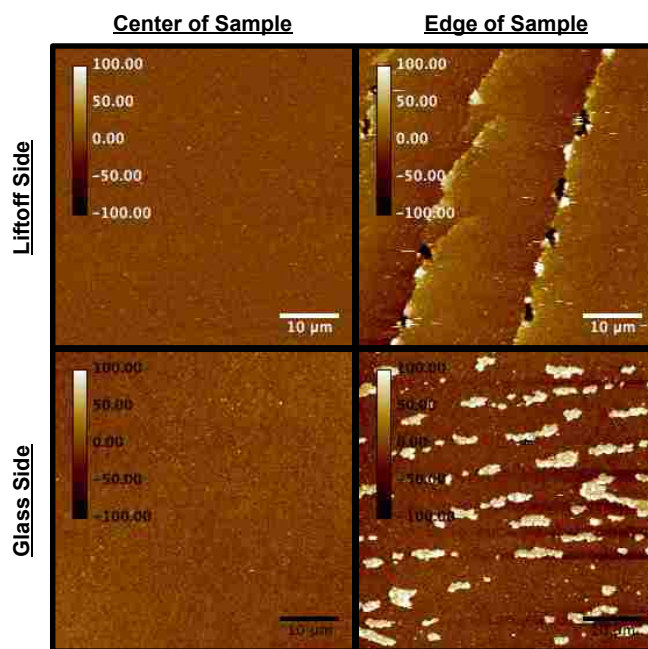
Figure 5.2: C-AFM images of the Liftoff (upper) and Glass (lower) sides of the interface. Images indicative of the center (left) and near-edge (right) morphologies suggest smooth cleaving for the majority of the interface and tearing near the edges.

5.3.3   Chemical analysis

To determine the chemical properties of the interface we first investigate the C 1s and O 1s detailed regions (figure 5.3). The O 1s intensity is predominately found on the

glass side in a SnO_x chemical environment, as expected for a SnO_2 surface. A small amount of O is seen on the liftoff side in the form of C-O and O-H bonds, which may be due to residual glass cleaning solvents incorporated into the interface. Likewise, C is found mostly as adventitious carbon.
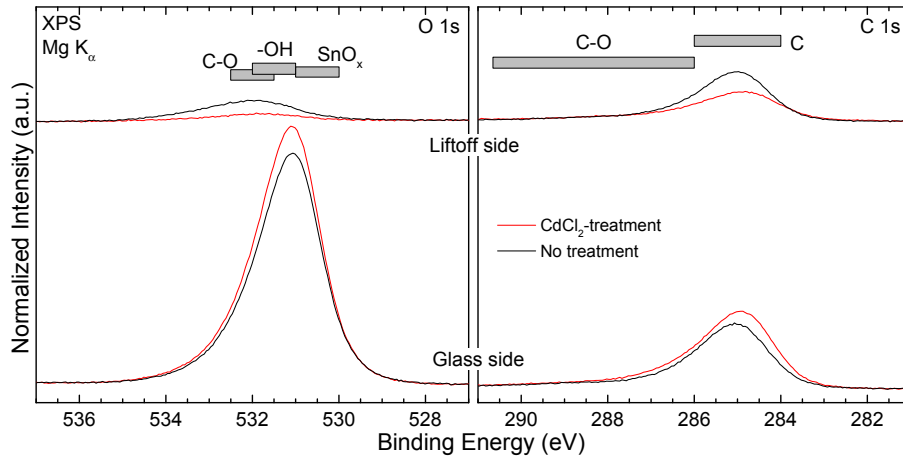
Figure 5.3: XPS detailed regions of the O 1s and C 1s photoemission.

CdCl$_2$-treatment effect the amount of C and O found at the sides of the interface, which can be attributed to the glass-cleaning step. To evaluate if this effect is due to changes in sample preparation or random changes a quantitative analysis is needed. For this the C 1s peak areas where integrated and compared across the interface and between samples. The integrated areas of the treated and non-treated are 3.359 and 3.364 ($\pm$ 0.005 a.u.), respectively, which is equal within the error of the integration and measurement. Given the samples where produced in one batch and the C 1s intensity is equal, the samples have equal amounts of "dirt" at the interface. The data from these two samples suggest once the layer stack is treated with CdCl$_2$, the C and O prefer to stick to the glass side of the interface, however a larger number of sample would be need to confirm the idea.

To confirm that the C and O are due to residual cleaning solvents SEM/EDX was used. Figure 5.4 shows SEM images excited with 5 keV electrons. Backscattered electron (BSE) signal (left), which is highly sensitive to atomic mass, shows features that are not present in the secondary electron signal, which is more sensitive to morphology. EDX (bottom) was performed on three features: a baseline (red), a surface spot feature (black), and an island (blue). The baseline, which comprised the majority of the surface, is largely SnO_x with some C and N. The surface spot has a significant increase in C signal while other emission lines remain constant. This would suggest residual solvents remain on the surface of the SnO_2 after cleaning, which is in agreement with intensity changes in the BSE image. C has a significantly smaller atomic mass than Sn, therefore the likelihood of an elastic scattering event (backscattering) is decreased, which results in a lower intensity area. Lastly, an island-like feature was measured with EDX and found to be $(Mg,Si)O_x$. This is likely a piece of the glass substrate that found its way to the glass side surface during the cleaving process. A Si signal is found with XPS on all surfaces in extremely small amounts, which is likely due to these glass fragments.
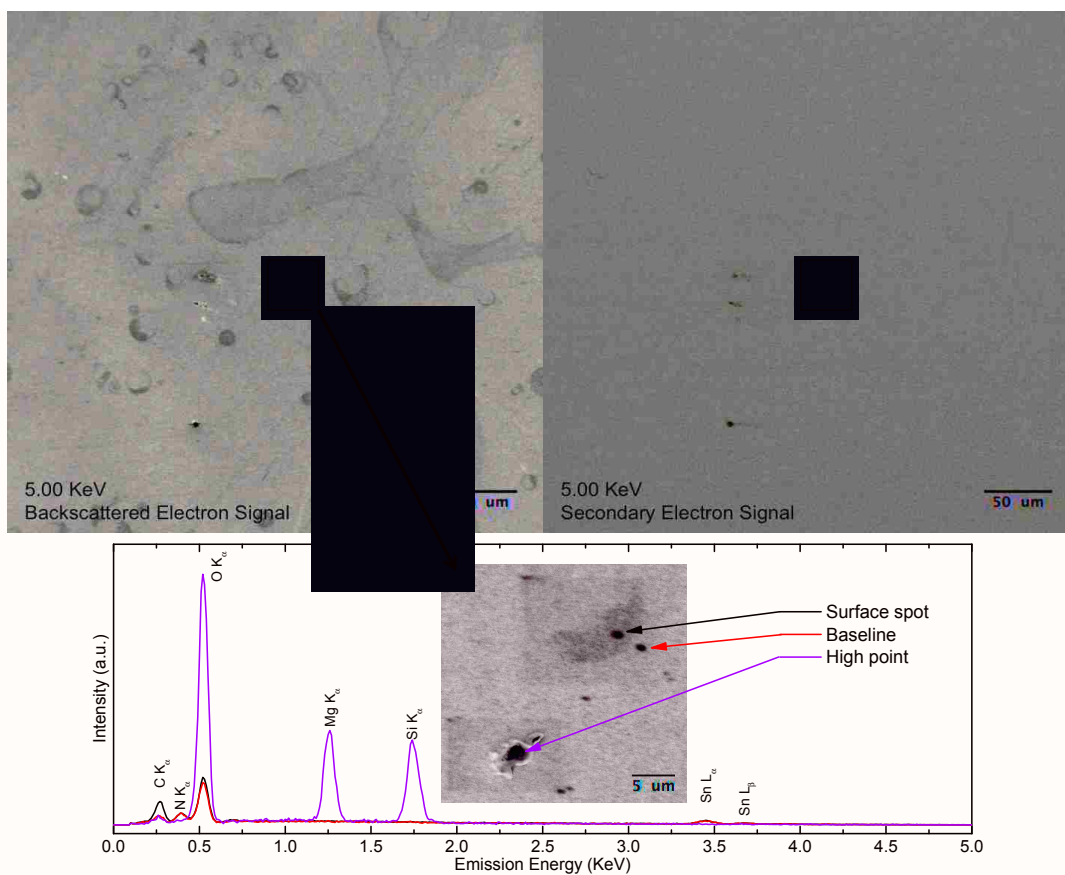
Figure 5.4: SEM/EDX measurements of a freshly cleaved layer stack. Backscattered electron signal (upper left) shows spot-like and island-like features, while secondary electron signal (upper right) only shows the island-like features, which suggests the spots are chemically different than the surface. EDX measurements (bottom) on an island-like (blue), spot-like (black), and surface (red) region indicate the island-like region to be glass and the spot-like region to have increased C signal. Black ovals on the inset image are carbon deposits due to EDX e-beam exposure for extended times.

Cl has long been known to penetrate along the grain boundaries, which enhances interdiffusion at the CdS/CdTe interface.[44] Furthermore, catastrophic adhesion failures are sometimes encountered at high CdCl$_2$ exposure levels.[47] In this study, Cl is found to diffuse to the CdS/SnO$_2$ interface.

To examine the chemical states at the interface, the core level spectra of elements associated with the liftoff side of the cleave, Figure 5.5, were investigated. First we study the liftoff spectra, and the glass side will be discussed later. By evaluating intensities, it is

seen that little Te is found at the CdS/SnO$_2$ interface prior to CdCl$_2$-treatment. The CdS film thickness (~100 nm) should be significantly thick to not have any appreciable amount of photoelectron signal for the CdTe sublayer. Te found at the interface suggests that diffusion caused by deposition at elevated temperature leads to the presence of Te throughout the entire CdS layer. After treatment a significant increase in Te signal is found, which suggests some Te has diffuses completely through the CdS layer. The Te 3d$_{3/2}$ peak position is consistent with bulk-like CdTe[38, 41] and it is important to note no TeO$_x$ is found at the interface. Which indicates adequate measures where used to prevent the surface from oxidizing after cleaving and more importantly oxides are likely not incorporated into the device.

A single intense peak is found for the non-treated liftoff side S 2s spectra. The binding energy of the S 2s peak corresponds to CdS and supports the assertion the oxides were not incorporated into the device. When the device is treated with CdCl$_2$ S 2s in found to decrease, which is expected since it is well known the S diffuse into the CdTe layer and even makes it to the surface of the CdTe.

A shift to higher binding energies in the chemical environment of the Cd 3d$_{3/2}$ peak is seen when treated with CdCl$_2$. This shift is consistent with Cd moving from a CdS or CdTe chemical environment to CdCl$_2$. Furthermore, a small decrease in intensity found. This may be due to a change in attenuation length, atomic concentration, and/or diffusion into the SnO$_2$:F substrate.
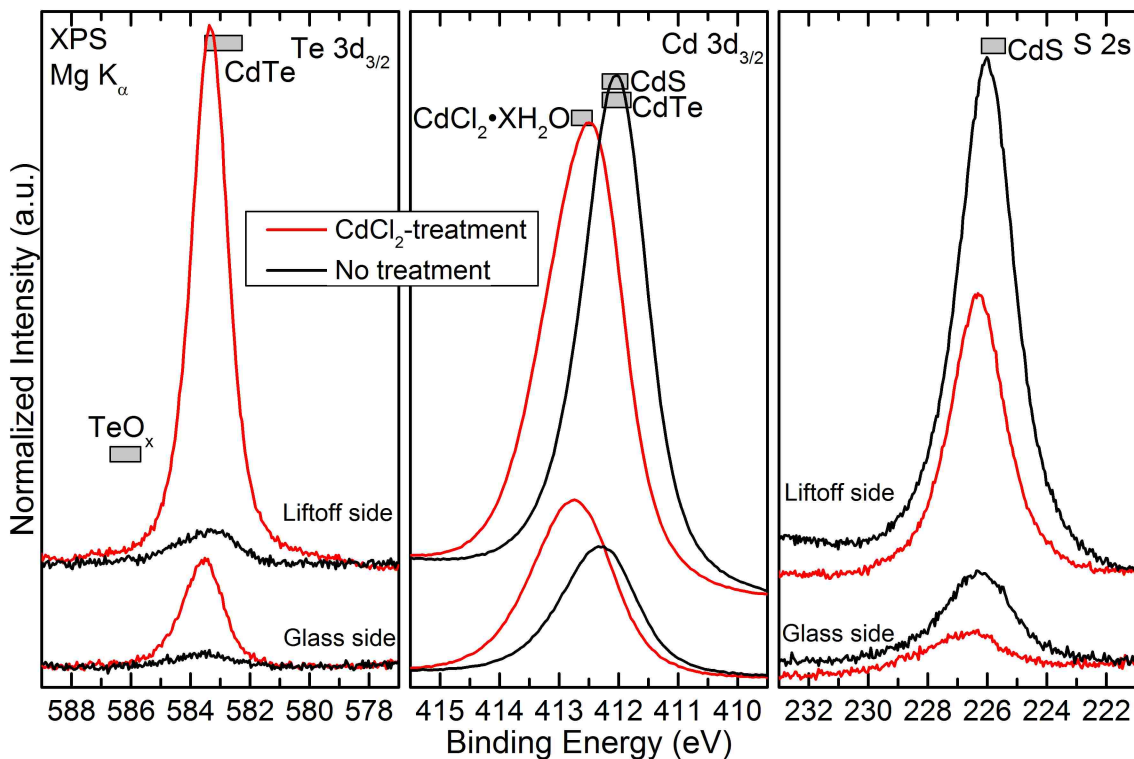
Figure 5.5: XPS detailed measurements of the Te 3d$_{3/2}$ (left), Cd 3d$_{3/2}$ (center), and S 2s (right) regions. Sample treated with CdCl$_2$ are shown in red, and spectra are separated into liftoff (top) and glass (bottom) sides. Binding energies of likely chemical states are depicted as grey boxes.

On the glass side of the interface a similar shift (to higher binding energy) is found for the Cd 3d$_{3/2}$ peak due to a change from CdS/CdTe chemical environment to CdCl$_2$. The presence of Cd at the surface of the glass side of the interface suggests Cd is diffusing into the SnO$_2$:F layer. An increase in Cd signal is seen after treatment with CdCl$_2$, which suggest the presence of CdCl$_2$ on the glass side as well for the liftoff side. As for S and Te similar intensity changes are found suggesting further diffusion into the SnO$_2$:F layer.

A similar evaluation is performed on the elements associated with glass side layers (Figure 5.6). Here we first evaluate the glass side elements. Both O 1s and Sn 3d$_{5/2}$ peak locations are consistent with SnO$_x$.[26, 38-39] The intensity of the peaks increase with

CdCl$_2$-treatment. On the liftoff side of the interface, O 1s is extremely weak and in an organic-like chemical environment, which is likely due to residual cleaning agents (see above). Sn is found to be in either a SnO$_x$ or Cd$_x$SnO$_y$ chemical environment prior to treatment and is not present after treatment. Together with liftoff side elements start to paint a picture of elements diffusing at both SnO$_2$:F/CdS and CdS/CdTe interfaces.
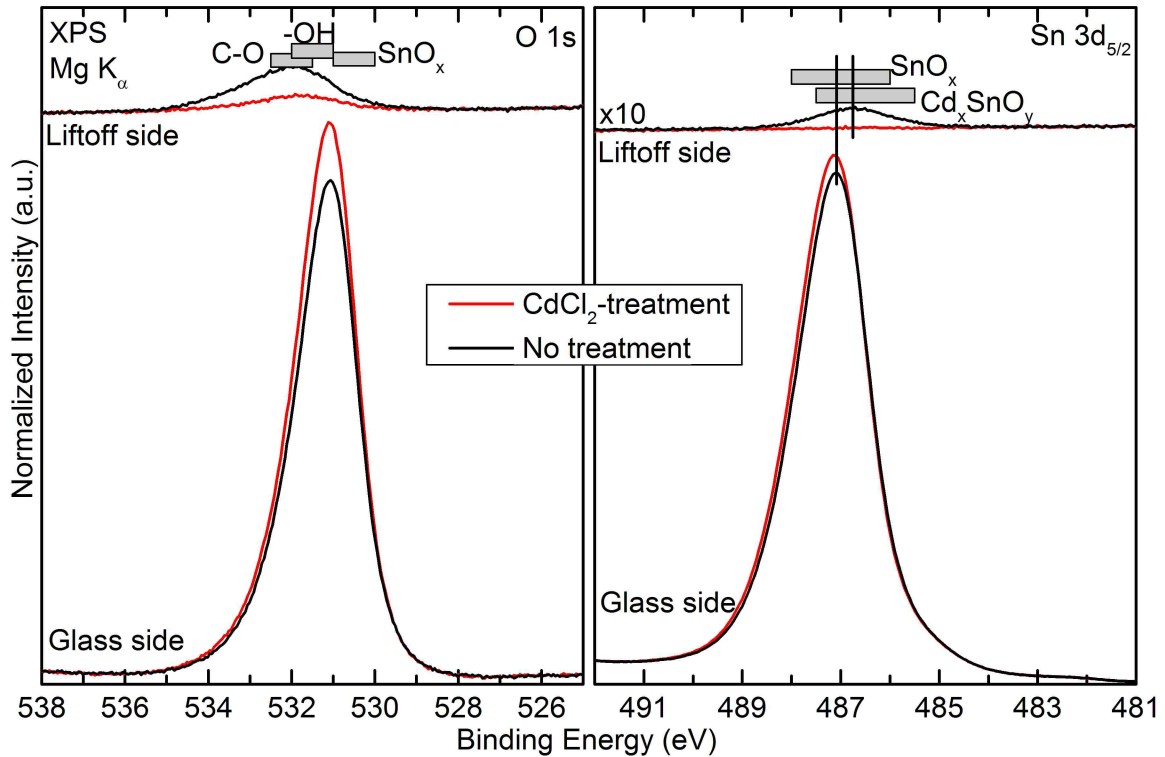
Figure 5.6: XPS detailed measurements of the O 1s (left) and Sn 3d$_{5/2}$ (right) regions. Sample treated with CdCl$_2$ are shown in red and spectra separated into liftoff (top) and glass (bottom) sides. Binding energies of likely chemical states are depicted as grey boxes.

Finally, we investigate Cl (Figure 5.7), which is associated with both surfaces. Cl is strongly found at both surface of the interface after CdCl$_2$-treatment. Previous studies have shown a delamination of the device if it is over treated with CdCl$_2$. A layer of CdCl$_2$ forming at the interface may explain the delamination. It is also interesting to find CdCl$_2$ at the interface of a non-treated sample. This is likely due to the production method of

multiple CSS pockets in one vacuum chamber. It is likely that $CdCl_2$ is found as a gas in the chamber and coats the device even if it is not directly above the evaporant.
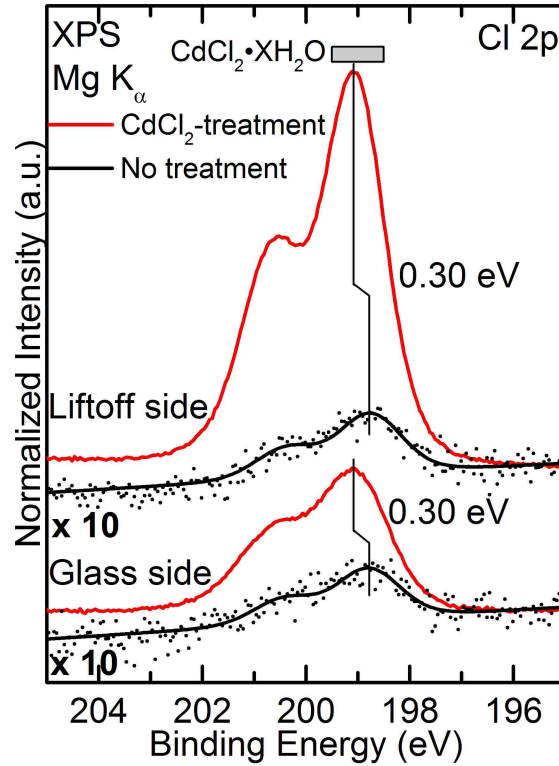
Figure 5.7: XPS detailed measurements of the Cl 2p region. Sample treated with $CdCl_2$ are shown in red and spectra separated into liftoff (top) and glass (bottom) sides.

5.4 Summary

By separating a layer stack at the SnO_2:F/CdS interface, much can be learned about the effects of $CdCl_2$-treatment on diffused species. By investigating the morphology, it was found that the center of the samples are smooth and an organic layer is present at the interface that is likely due to residual organic cleaning solvents prior to film deposition. By incorporating a plasma-cleaning step to remove residual organics device, our partners were able to improve device performance.

XPS was used to probe the chemical environment of the interface and significant amounts of diffusion is found at both SnO_2:F/CdS and CdS/CdTe interfaces before and

after CdCl$_2$-treatment. Further work is need to determine the extent of these diffused species. However, one can conclude that the simple heterojunction band alignment picture is not sufficient to describe the interactions of the TCO/Buffer/Absorber layers in a CdTe-based photovoltaic device.

CHAPTER 6   CHARACTERIZATION OF THE SULFUR BONDING IN CdS:O

BUFFER LAYER FOR CdTe-BASED THIN-FILM SOLAR CELLS

The following chapter is previously published in ACS Applied Materials and Interfaces and reports work performed to study the chemical and electronic properties of alternative buffer materials. Reprinted with permission from D. A. Duncan, J. M. Kephart, K. Horsley, M. Blum, M. Mezher, L. Weinhardt, M. Häming, R. G. Wilks, T. Hofmann, W. Yang, M. Bär, W. S. Sampath, and C. Heske, Characterization of Sulfur Bonding in CdS:O Buffer Layer for CdTe-Based Thin-Film Solar Cells, *ACS Appl. Mater. Interfaces* 2015,7, 16382-16386. Copyright 2015 American Chemical Society.

6.1 Introduction

While Si-based devices currently dominate photovoltaic power production, thin-film devices based on CdTe have achieved a notable market share as a cost-effective alternative (with current world-record cell efficiency of 21.0%)[1]. For further improvement, efforts focus on the fact that absorption in the CdS buffer layer of such cells reduces the flux of high-energy photons to the CdTe absorber. This parasitic light absorption can result in more than 10% loss in short-circuit current density.[2] One way to prevent this loss is to increase the band gap of the buffer material, e.g., by incorporating oxygen during RF sputtering of CdS (such as by introducing O_2 into the Ar flow).[3-5] A similar method has been successfully used for chalcopyrite thin-film solar cells.[48-50] For CdTe, this process has produced devices with efficiencies above 15%.[3, 5] In order to optimize the buffer properties and to further improve device performance, a detailed understanding of the electronic and chemical structure is required. Experiments by Soo, et al. [51] have shown the bulk of such films to consist of oxygen-free CdS nanocrystals and

S-O complexes, which are speculated to be SO_3^{2-} and SO_4^{2-} complexes.[51] To analyze the chemical structure of the S-O complexes in detail, x-ray photoelectron spectroscopy (XPS) and soft x-ray emission spectroscopy (XES) were used to study the species-specific composition of the surface and bulk, respectively. We thus derive the impact of oxygen incorporation into CdS thin films, monitoring the relative intensities of the various sulfur species at the surface and bulk as a function of O content. The results allow for deeper insights into, and deliberate optimization of, such CdS:O thin films in solar devices.

6.2 Experimental Details

CdSO$_x$/SnO:F/glass layer stacks were grown at CSU using RF sputtering. O_2 gas (99.999%) was introduced into the Ar flow of the sputter gas. Based on deposition time, the expected thickness of the CdSO$_x$ films is 100 nm. The amount of O_2 incorporated is related to its flow rate relative to Ar. One sample was produced with an O content corresponding to best in-lab devices (2.3% O_2 flow rate relative to Ar), one below (2.0%), and one above (2.5%). Substrates were Tec 10-coated 3.2 mm float glass acquired from Pilkington.[4-5] After production, the samples were vacuum-sealed under dry nitrogen, without exposure to air, and shipped to UNLV for characterization. The samples were unpacked in the inert environment of a dry nitrogen-filled glovebox and directly introduced into the ultra-high vacuum (UHV) system with a base pressure below 5×10^{-10} mbar. X-ray photoelectron spectroscopy (XPS) was performed using a twin-anode Al K_α/Mg K_α x-ray source (Specs XR-50) and a Scienta R4000 electron analyzer; the energy scale was calibrated in accordance with ISO 15472[22].

X-ray emission spectroscopy (XES) of the S $L_{2,3}$ edge was performed at Beamline 8.0.1.2 of the Advanced Light Source (ALS), Lawrence Berkeley National Laboratory, employing our SALSA endstation with a custom-designed, high-transmission soft x-ray spectrometer[35, 52]. To transfer the samples to ALS, they were vacuum-sealed without air exposure, unpacked in the inert environment of a dry nitrogen-filled glovebag and directly introduced into the experimental station (base pressure below 1 x 10^{-8} mbar). To minimize beam damage effects, the sulfite and sulfate reference powders were scanned in the beam.

6.3 Results and Discussion

Mg K_α XPS survey spectra of the as-received CdS:O surfaces (Figure 6.1) display all expected photoemission and Auger lines (of Cd, S, and O). We also find a small C 1s contribution, which is likely due to residual carbon contaminants in the 15 mTorr Ar environment of the CdS:O RF sputter deposition chamber. The intensities were magnified by a factor of 5 for binding energies below 250 eV to show a splitting of the S 2s and 2p lines, which will be discussed in more detail in the following. Furthermore, we find that the O 1s signal increases and the Cd signals decrease in intensity with increased oxygen flow rate, as expected, and observe the presence of a Cl contamination on the 2.5% sample.
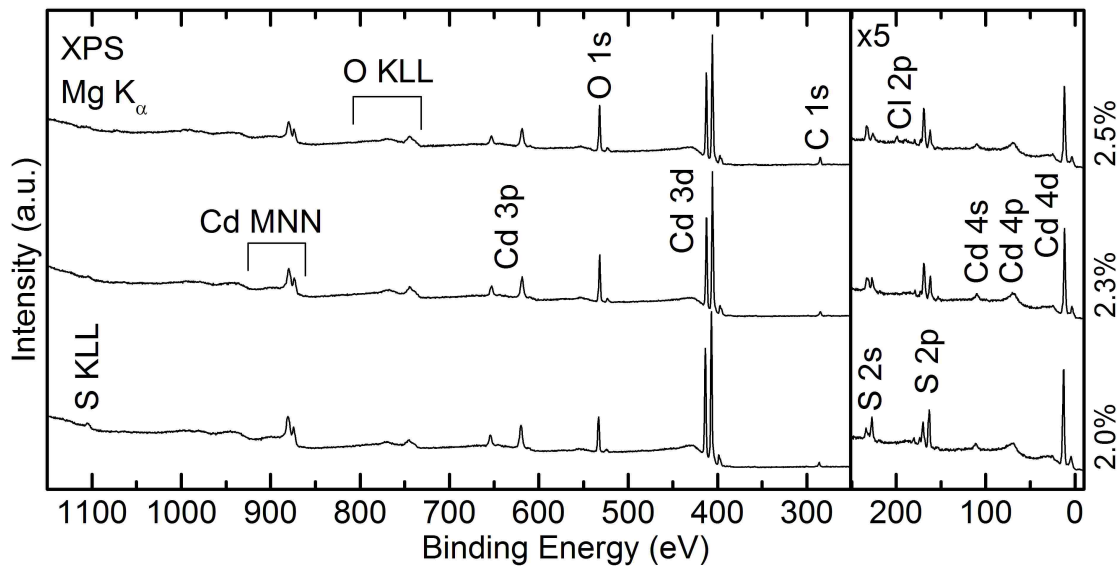
Figure 6.1: Mg K_α XPS survey spectra of three CdS:O films with O_2/Ar flow rate ratios of 2.0, 2.3, and 2.5% (as labeled on the right ordinate). All photoemission and Auger electron emission lines are labeled, and the spectra are magnified by a factor 5 for

A detailed measurement of the S 2p region (Figure 6.2, blue circles) suggests the presence of at least three sulfur species. In order to analyze the relative binding energy differences between them, the peak center of the lowest-binding energy species

(attributed to CdS) was set to zero in all spectra, requiring spectral shifts of 1.5 eV or less. This approach also mitigates any impact of surface band bending, doping, and (if present) charging effects. At high binding energies, the spectra are comprised of S 2p atoms consistent with a CdSO4 environment15 (green), ~7 eV shifted w.r.t. CdS (red), and an intermediate oxide shifted by ~6 eV and labeled "$CdSO_x$" (blue). The chemical shift of this intermediate oxide is consistent with other sulfite species[26, 39], but it requires a detailed analysis of the XES spectra (see below) to derive additional evidence to suggest that this species is indeed a $CdSO_3$ (note that no XPS reference spectra for CdSO3 could be found in an extensive literature search). For the three samples it is seen that, roughly, the CdS contribution decreases and the $CdSO_4$ contribution increases with increased oxygen flow rate, as expected. The intermediate oxide, $CdSO_x$, remains approximately constant despite the increased oxygen incorporation.
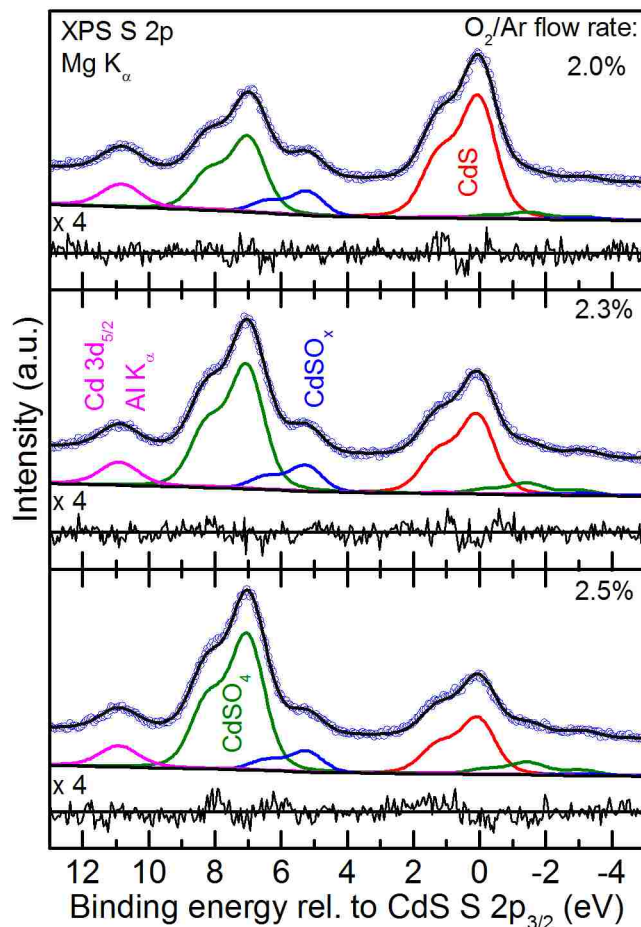
Figure 6.2: S 2p Mg K α XPS spectra (blue dots) of three CdS:O films with O_2/Ar flow rate ratios of 2.0, 2.3, and 2.5%. The spectra are referenced to the binding energy of the S $2p_{3/2}$ line of CdS, and described by spectral components representing CdS (red), $CdSO_X$ (blue), CdSO4 (green), Cd $3d_{5/2}$ (excited by Al K α, magenta), and the sum of the fit functions (overlaid with the blue dots of the data). Each component consists of two Voigt functions describing the S 2p spin-orbit doublet and a contribution at lower binding energies originating from the Mg K $\alpha_{3,4}$ satellites excitations of each line. Below each spectrum, the residuum of each fit is shown, magnified by a factor of 4

In order to derive a detailed quantification, we note that it is not feasible to simply integrate the area under the spectra, since the lines of the different sulfur species overlap. Instead, a detailed and thorough fit analysis, using a sulfur spin-orbit doublet for each species, is required. Furthermore, all three spectra need to be fitted simultaneously, for which we used the Fityk fitting software[29]. Each species in figure 6.2 was described by a sum of eight coupled Voigt functions (red, green, and blue lines) to account for the spin-

orbit splitting (with a ratio of 2:1 for the S $2p_{3/2}$ and $2p_{1/2}$ line, resp.) and to include the Mg $K_{\alpha1,2}$ main line as well as the $K_{\alpha3,4}$ satellite excitations. The relative areas and energies were set according to Moulder, et al. [38], while the Gaussian and Lorentzian widths, resp., were identical for all species (and used as two free fit parameters). A linear background was simultaneously fitted, and a small Al K_{α}-excited Cd $3d_{5/2}$ photoemission peak (magenta) was also included to account for a small x-ray source crosstalk. In total, the three spectra were simultaneously fitted with 20 free parameters (out of a total of 480 variables). The resulting fits give an excellent description of the experiment, as is evidenced by the largely statistical nature of the residua shown under each spectrum (magnified by a factor of 4) in Figure 6.2.

The surface composition (Figure 6.3, left ordinate) was calculated using the area percentage of the different species in the fit. The CdS and $CdSO_4$ composition at the surface both have a linear dependence on O_2/Ar flow rate across this range, while the intermediate, $CdSO_x$, is constant. In this particular series, films leading to the best solar cell performance were made with a 2.3% O_2/Ar flow rate, which, according to Fig. 6.3, represents a slightly $CdSO_4$-rich surface. A detailed analysis of the impact of various preparation parameters on solar cell performance in other sample series is given in Kephart, et al. [5]
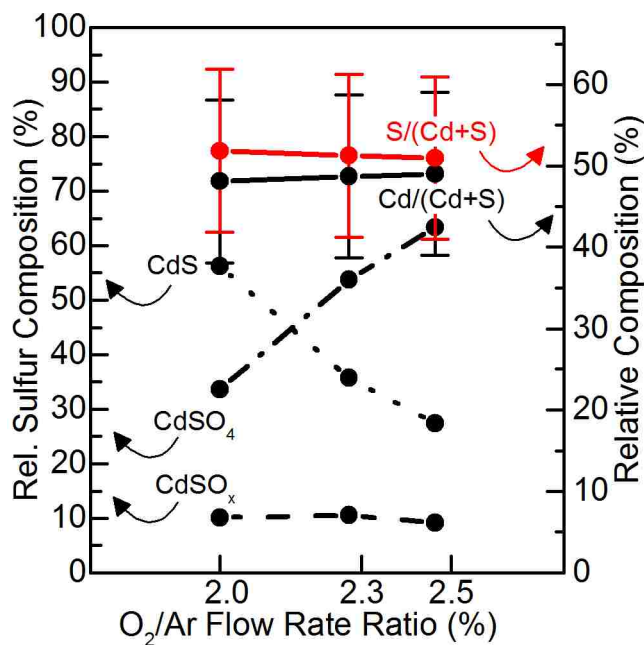
Figure 6.3: Left ordinate: relative sulfur composition for the CdS (dotted), CdSO$_4$ (dash-dotted), and CdSO$_x$ (dashed) spectral component as a function of O$_2$/Ar flow rate ratio. Error bars (not shown) are ±2 abs% or less. Right ordinate: Relative composition of Cd (Cd/(Cd+S), black) and S (S/(Cd+S), red) for all three samples.

To determine the relative composition of S and Cd, we have analyzed the intensity of the Al K$_\alpha$-excited Cd 3d$_{5/2}$ line and the total S intensities by using calculated cross sections[40], taking the relative intensity of the Al K$_\alpha$-excitation into account (as derived from a separate measurement of a gold reference), and by assuming that the transmission function and attenuation lengths are constant over this narrow energy window. We find that the relative composition of Cd and S (Figure 6.3, right ordinate) is varying only slightly for the three samples (and well within the error bars of determining the *absolute* values). This indicates that, at increasing O$_2$ flow rates, no significant formation of other oxygen-containing cadmium species (e.g., CdO or Cd(OH)$_2$) is found (if present, this would lead to a variation of the Cd/S ratio). Instead, increased O$_2$ flow

rates apparently lead to the formation of oxide species that include both sulfur and cadmium.

To gain more detailed insights into the chemical environment of the sulfur atoms, in particular regarding the intermediate oxide, we recorded S $L_{2,3}$ x-ray emission spectra using high-brilliance synchrotron radiation.

For CdS, the 1/e-attenuation length of the exciting (200 eV) and emitted (ca. 150 eV) photons are approx. 100 and 370 nm, respectively.[33] For $CdSO_4$, the corresponding values vary according to the degree of hydration (and thus density), but range from 120 to 192 nm at 200 eV, and from 193 to 247 nm at 160 eV (i.e., the approximate emission energy for the sulfate spectrum).[33] The investigated films are approx. 100 nm thick; thus, the XES spectra contain information from both, the surface and the bulk of the film (with an exponential weight distribution).

Figure 6.4 shows S $L_{2,3}$ emission spectra of the three films, as well as references for a sulfide (CdS), sulfite (Na_2SO_3) and sulfate ($CdSO_4$) species. S 3s electron decays are seen in two energy regimes.[53-56] For CdS, the broad feature at 147.5 eV is a convolution of the two "S 3s to S $2p_{1/2}$ and $2p_{3/2}$" decay channels in a CdS-like chemical environment. Transitions of S 3s electrons in a $CdSO_4$ chemical environment emit photons at 153.9 and 155.1 eV. Cd 4d-derived valence state decays are also present in both chemical environments, namely at 150.4 and 151.6 eV for CdS and (much less pronounced) at ~156.5 eV for $CdSO_4$. The peak at 161.0 eV, assigned to S 3d states, is only present in the $CdSO_4$ chemical environment.
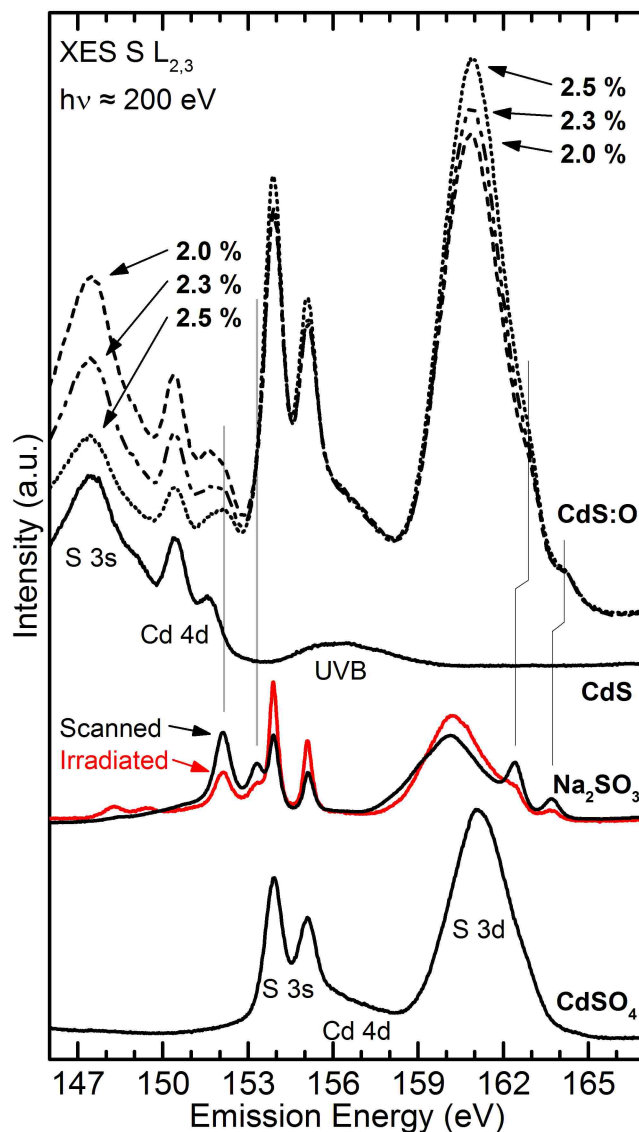
Figure 6.4: S $L_{2,3}$ x-ray emission spectra of the three CdS:O films with O_2/Ar flow rate ratios of 2.0, 2.3, and 2.5% (top), compared to CdS, $CdSO_4$, and $NaSO_3$ powder references. For the latter, two spectra are shown: with minimal ("scanned") and substantial ("irradiated") beam exposure. Peak labels refer to bands and/or valence orbitals with a strong contribution from the given atomic levels.

To also gain insights into the possible presence of a sulfite species, we note that $CdSO_3$ is highly unstable and that we therefore used Na_2SO_3 as a reference. The sulfur atom in Na_2SO_3 is predominantly bonded in a molecular fashion, suggesting that the S $L_{2,3}$ emission spectrum of Na_2SO_3 is also a good representative for $CdSO_3$. This

assumption is supported by the fact that various different sulfate S $L_{2,3}$ emission spectra look very similar as well (Figure 6.5). The Na_2SO_3 reference shows a variety of additional peaks, in particular a series of peaks between 151 and 155 eV, as well as two peaks at 162.5 and 163.7 eV, respectively. In order to identify peaks pertaining to pristine Na_2SO_3, Figure 6.4 shows two spectra, one recorded with minimal beam exposure by scanning the sample ("scanned"), and one after substantial beam exposure, indicating beam induced changes in the reference sample ("irradiated").
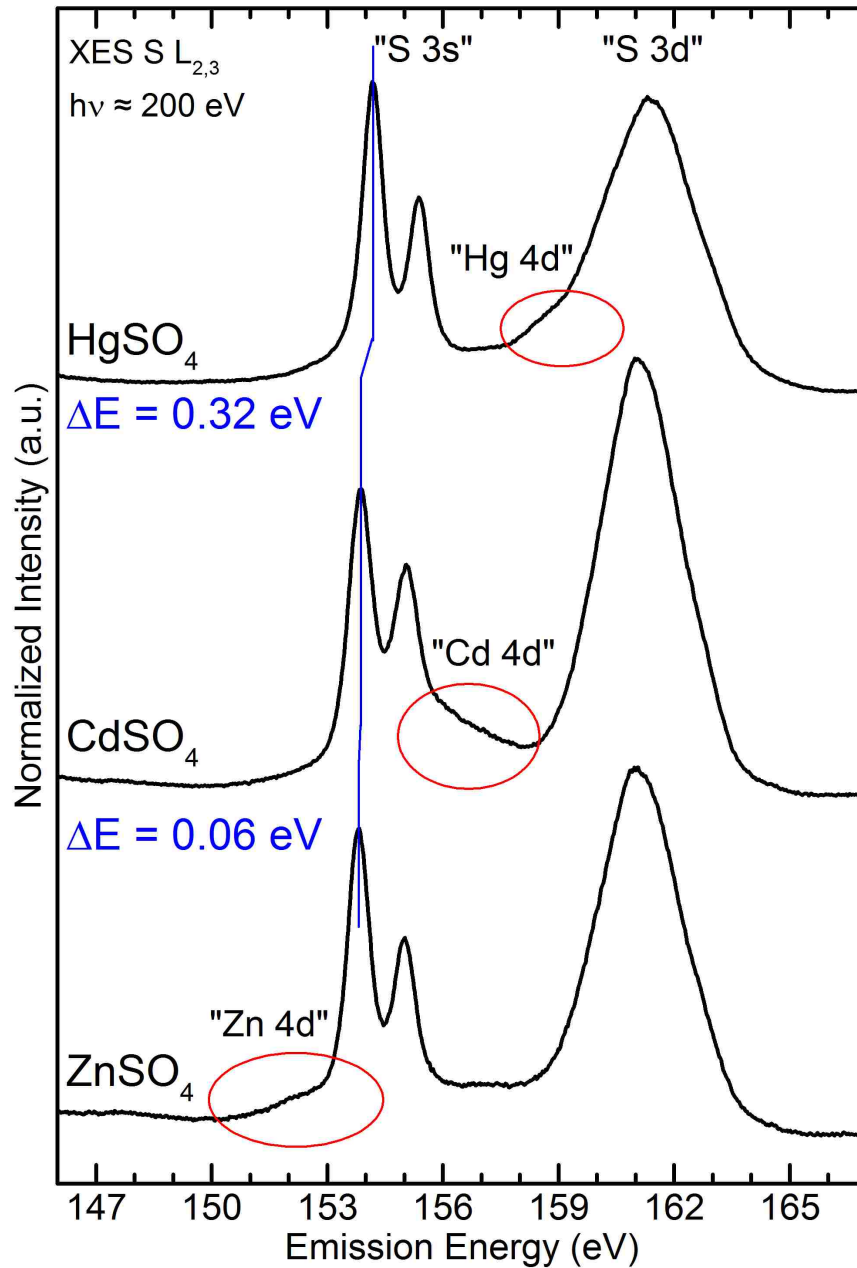
Figure 6.5: S $L_{2,3}$ emission spectra of $HgSO_4$, $CdSO_4$, and $ZnSO_4$ (top to bottom). S 3s and S 3d decays are found to maintain shape and relative locations due to the molecular nature of the orbital. Metal 4d decays are found to shift to higher emission energies with increased atomic number.

A closer look at the three S $L_{2,3}$ spectra of the here-studied films (top three spectra in Fig. 6.4) reveals a character that is primarily described as a superposition of a sulfide

and a sulfate species. Small deviations are found near 152.1 and 153.3 eV, as well as near 162.9 and 164.1 eV. These are ascribed to the most prominent (additional) peaks in the sulfite spectrum, as indicated by the thin vertical lines. Small differential shifts are speculated to be due to a different (molecular) character of the sulfite under study. As indicated by the arrows in Fig. 6.4, an increase of the O_2 flow rate leads to a reduction of the sulfide component and an increase of the sulfate component, while no evidence for a significant change in sulfite contribution can be observed. This is in direct agreement with the findings based on the XPS data of the thin-film surfaces, which exhibit an even larger increase in the sulfate component than the bulk-sensitive XES measurements. This could be due to depth-dependent variations in the composition of the film, but an impact of the XES excitation (i.e., a "sulfate breeding"[57]) can also not be ruled out.

Nevertheless, the existence of three sulfur species (sulfide, sulfate, and intermediate) is found in both XES and XPS, and the comparison with the sodium sulfite reference suggests that the intermediate species might indeed be described as a sulfite (while additional, more complex sulfur compounds could, of course, also be present). By having identified the various components and their relative compositions as a function of O_2 flow rate, it is now possible to optimize performance of novel CdS:O films, as well as to complement such activities by suitable structure and electronic models based on the species composition of the CdS:O films.

6.4 Summary

We have studied the chemical and electronic structure of CdS:O thin films produced by incorporating O_2 into the Ar gas flow during sputter deposition. The surface was investigated by XPS, while the bulk of the films were studied by XES. The films

were found to be mainly comprised of CdS and $CdSO_4$, with small additions of an intermediate $CdSO_x$ (most likely sulfite) species. With increasing oxygen incorporation, $CdSO_4$ is the preferred species, at the expense of CdS, while the content of the intermediate oxide species remains constant. As the oxygen incorporation into the CdS:O films serves several purposes, it is important to understand the composition of such films not just on an atomic level (i.e., composition of Cd, S, and O), but also from the view point of concentration of particular species (i.e., sulfide, sulfate, and intermediate oxide). With such insights, it is now possible to establish suitable models for the CdS:O film properties and their impact on the performance of high-efficiency thin film solar cells. Furthermore, empirical tailoring towards the optimal balance between the different species can now be quantified and solar cell optimization is thus greatly facilitated.

CHAPTER 7   THE CHEMICAL AND ELECTRONIC STRUCTURE OF

$Zn_{(1-x)}Mg_xO/CdTe$

7.1 Introduction & Sample Preparation

$Zn_{(1-x)}Mg_xO$ "(Zn,Mg)O" is proposed as an alternative buffer layer to CdS. (Zn,Mg)O has a tunable band gap of 3.3 - ~4 eV which makes it a great candidate to replace CdS.[19] First Solar Inc. has begun studying the effects of implementing ZMO into test devices; a fundamental understanding of the chemical and electronic properties may aid in optimization. Specifically, a strong understanding of the interface band alignment will help optimize the short circuit current of the device.

To study the interface, 20 nm thick $Zn_{(1-x)}Mg_xO$ were grown on SnO_2-coated glass using atomic layer deposition (ALD). The samples were quickly transferred (in air, ~3 min) to a separate growth chamber where CdTe was deposited by thermal evaporation. The growth time was adjusted for the sample in order to grow 2 nm, 5 nm, and 10 nm thick CdTe films. After growth all samples were packaged in the inert environment of an N_2-filled glovebag, which was directly attached to the deposition chamber. A bare (Zn,Mg)O film was grown and packaged with the same process during a separate experimental run (including short air exposure before packaging). Upon delivery to UNLV, the samples were immediately moved to an N_2-filled glovebox.

7.2 Chemical Properties

The Al K_α XPS survey spectrum of the as-received bare substrate surface (Figure 7.1) displays all expected photoemission and Auger lines (Zn, Mg, O), which decrease in intensity with increasing CdTe overlayer thickness. Cd and Te lines are found on the 2 nm film and increase in intensity with thicker CdTe layers (also Fig. 7.1). We also find a

small amount of C on all samples. The spectra in Fig. 7.1 are magnified by a factor of 3

for binding energies below 250 eV to show intensity changes of the shallow core levels.
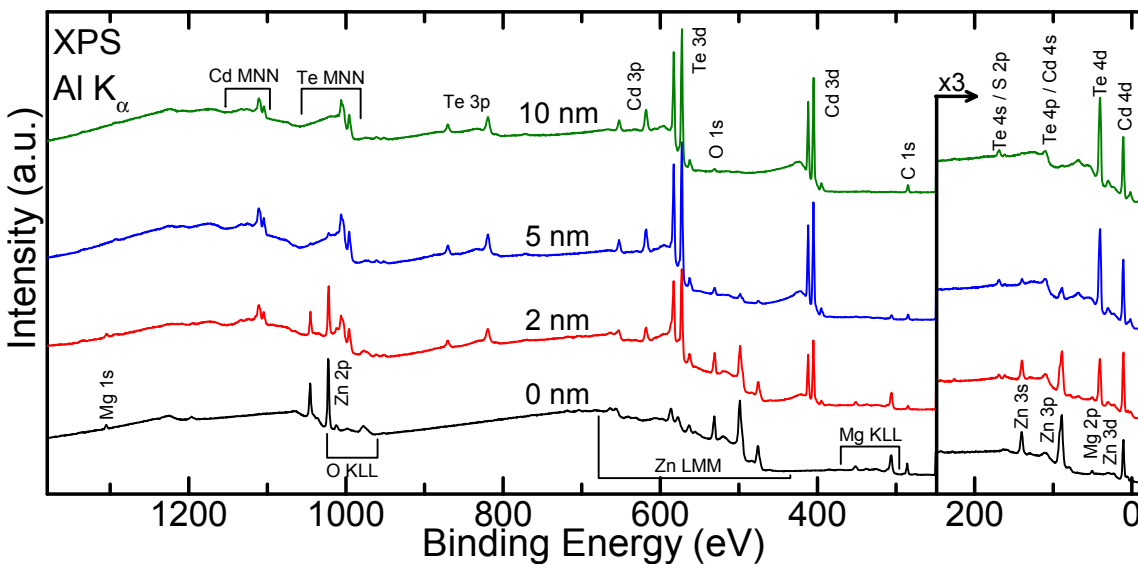
Figure 7.1: Al K$_\alpha$-excited XPS survey spectra of the bare ZMO film ("0 nm," black), as well as the thin ("2 nm," red), intermediate ("5 nm," blue), and thick ("10 nm," green) CdTe film grown on ZMO. The lower binding energy regions are magnified (x3) to better see shallow core level peaks.

To confirm the presence of S on the surface of all samples the S Auger was also

investigated (Figure 7.2). Auger intensity was found on all samples, which confirms the

presence of S at/near the surface. It was also seen that the overall intensity decreases with

thicker CdTe layers. Two peaks are found in the S Auger region. The first peak at 154 eV

is present on all samples, while the second at 152 eV is most intense for the bare

(Zn,Mg)O film and decrease with the addition of CdTe film. This second peak is within

the noise of the 10 nm CdTe. Usually the S KLL Auger is used for chemical analysis so

little work is published on the S LMM peak positions. Therefore, the S 2p peaks will be

used to gain insights to the S chemical environments.
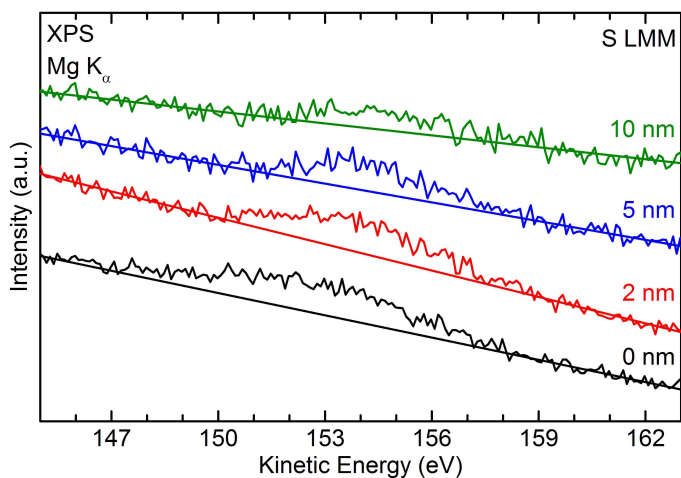
Figure 7.2: XAES detailed spectra of the S LMM region.

A detailed measurement of the S 2p / Te 4s region (Figure 7.3, black dots) shows at least four photoemission peaks. At 161 eV, a doublet, consistent with a sulfide (likely CdS and/or ZnS)[21, 38-39] is found on all CdTe containing surfaces. Although two peaks are found for the S LMM Auger only a single doublet is needed to adequately describe the S 2p spectra. The S 2p intensity increases with the initial addition of CdTe and then decreases with increasing film thickness. At 169 eV, the Te 4s peak increases in intensity with increasing film thickness, as expected, and an Al K_α-excited Cd $3d_{5/2}$ peak, at 173 eV, is found due to a small amount of x-ray source crosstalk. Sulfur can cause diffusion and band gap grading in conventional devices[58], therefore care must be taken when interpreting the derived band gaps and level alignments in later discussions (Chapter 7.4).
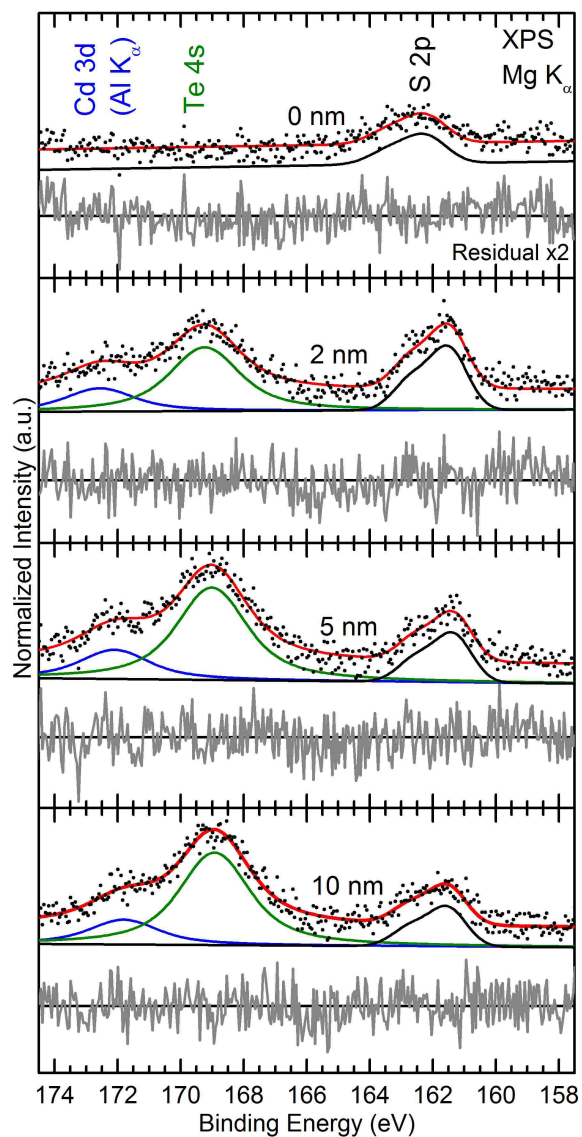
Figure 7.3: XPS detailed measurement of the S 2p / Te 4s region. Spectral data (black dots) where fit using Voigt functions representing S 2p (black), Te 4s (green), and Cd $3d_{5/2}$ (blue). The difference of data and the sum of Voigt functions (Fit, red line) is magnified by 2 and plotted below each data set (grey line).

To further explore the chemical properties at the interface, the Te $3d_{5/2}$ region was investigated (Figure 7.4). By plotting the spectra over each other and normalizing them to the peak maximum small changes in spectral shape are best seen. Two differences between the spectra are found. The first difference is a peak found at 586.6 eV on the 5

and 10 nm CdTe films that is consistent with Te in a TeO_x chemical environment. The second difference is a broadening of the 2 nm peak to higher binding energies (indicated by an arrow). To examine the energy and intensity differences between various peaks a careful fit analysis was performed.

The first attempt to effectively describe the data used three Voigt functions (Figure 7.4, left). All four spectra where fit simultaneously and the peaks shape and relative energy differences where set equal for all functions. The resulting functions (grey, red, and green regions) cannot adequately describe the data, as seen by an oscillating difference between data and fit (grey line). When a fourth Voigt function is added (Figure 7.4, right) the difference between data and fit significantly improves. The oscillations are no longer present and only random statistical variations are seen, which indicate at least four features are present in the spectra.

The relative contribution of the major component is found to increase with layer thickness, and the energy position is consistent with bulk-like CdTe. The smallest component is consistent with Te in an oxidized environment. It is unclear whether oxidation is a result of exposing the (Zn,Mg)O surface to air prior to CdTe deposition, diffusion from the (Zn,Mg)O substrate, or incorporation of O into the CdTe film during growth. A third and fourth component (peaks "A" and "B"), which describes the broadening seen in the 2 nm spectrum, decrease in intensity but do not completely go away with thicker CdTe films. The relative intensities change becoming slightly more peak "A" rich with increased CdTe film thickness.

The two most likely causes of peaks "A" and "B" are scattering and additional species. The most common scattering process takes place when an excited photoelectron

inelastically scatters a second electron into an unoccupied state. For the case of a semiconductor, the smallest transition a scattered electron can make is from the valence band maximum to the conduction band minimum (or the band gap, E_g). Therefore the energy difference between main peak and scattering feature must be $\geq E_g$ (1.5 eV for bulk CdTe[59]). Here, it is found the energy difference between the CdTe and "A" ("B") peaks are 0.57 (1.4) eV. This energy difference is too small to explain peak "A" as loss features, however peak "B" cannot be ruled out. When evaluating the two peaks as additional species "A" is consistent with bulk-like ZnTe[26, 38-39], and "B" is speculated to be MgTe, although no reference binding energies are published. The ratio of the MgTe/ZnTe, for the 2 nm sample, is consistent with the bulk stoichiometry of the (Zn,Mg)O substrate, which supports the identification of the "B" component and suggests the formation of a (Zn,Mg)Te at the interface. No evidence of chemical changes is observed for any other elements.
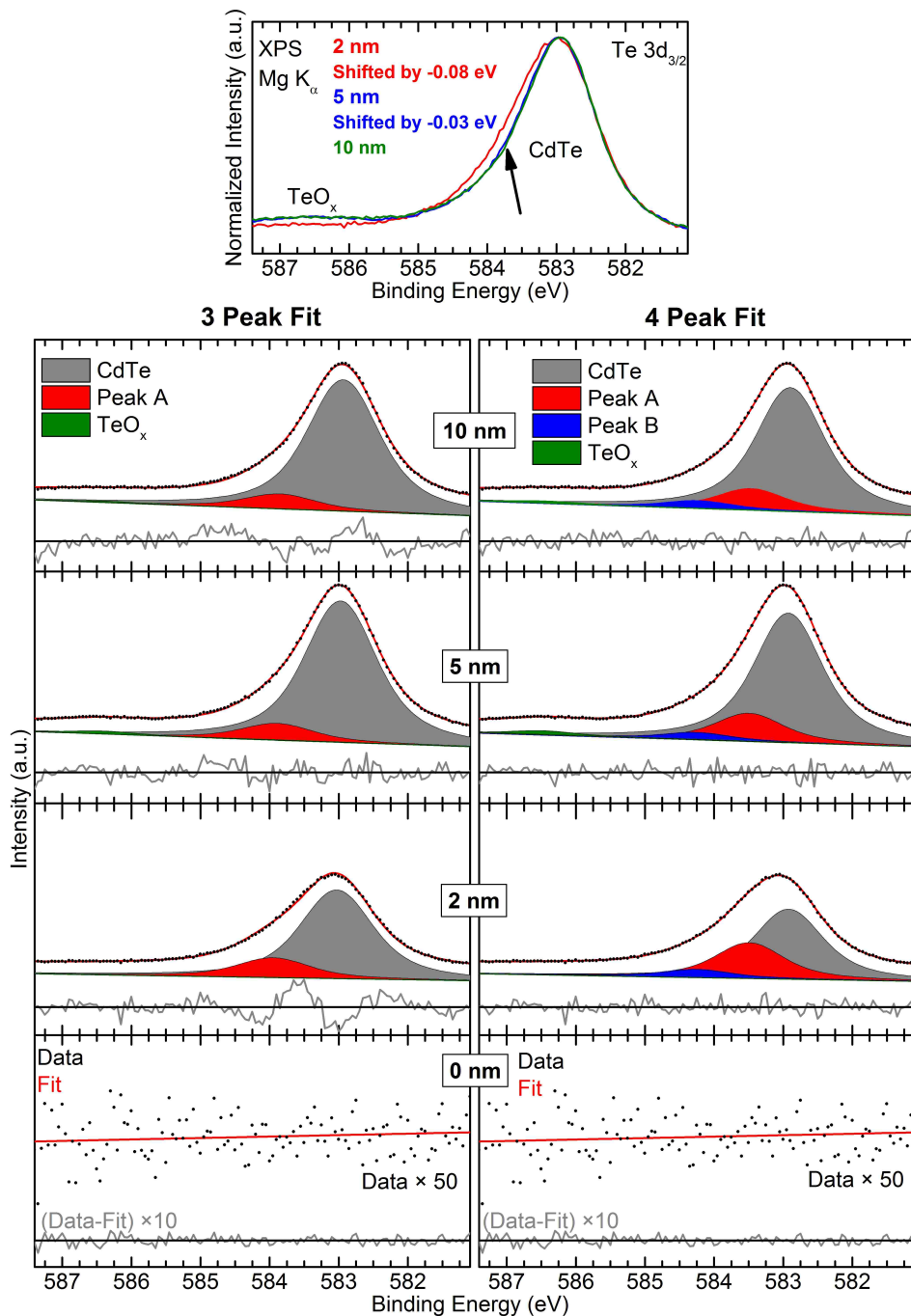
Figure 7.4: XPS Te $3d_{3/2}$ detailed region normalized to peak maximum (top) and fit with 3 peaks (left) and 4 peaks (right). For the two lower graphs spectral data (black dots) where fit using Voigt functions representing CdTe (black), ZnTe (red), MgTe (blue), and TeO_x (green). The difference of data and the sum of Voigt functions (Fit, red line) is magnified by 10 and plotted below each data set (grey line).

7.3 Band Bending

With close examination of all photoelectron and Auger peaks, systematic shifts are found likely due to interface and overlayer formation. Table 7.1 displays all major peaks and the shift relative to the bare (Zn,Mg)O and thick CdTe films for (Zn, Mg, O) and (Cd, Te), respectively. Peak positions were determined by fitting the data as described in section 3.1.6. Due to the short attenuation length of some high binding energy peaks and/or low photoionization cross-section, some intensities are too weak to confidently determine position and therefore marked "N/A" in Table 7.1. The final column "BB" indicates the average interface-induced band bending for the respective sample. Peaks associated with the substrate (Zn, Mg, O) display a 0.31 and 0.37 ± 0.05 eV upward interface-induced band bending (toward the Fermi energy) for the 2 and 5 nm thick CdTe films, respectively. A larger upward band bending is found for the 5 nm thick sample, which is likely due to the increased proportion of interface signal relative to the near-interface bulk signal of (Zn,Mg)O. Therefore the calculated band bending may be considered a lower bound to the "true" band bending at the interface. A similar upward shift of 0.13 and 0.07 ± 0.05 eV (2 nm and 5 nm, respectively) is found for overlayer peaks (Cd, Te) due to layer formation. Larger weight is given to the band bending values with a higher proportion of interfacial signal. Therefore, the best estimate for interface-induced band bending in the (Zn,Mg)O layer to be 0.35 ± 0.05 and band bending in the CdTe layer to be 0.11 ± 0.05 eV.

Table 7.1: All peak shifts associated to band bending. Shift values are relative to the 0 and 10 nm films for the substrate and CdTe peaks, respectively. Positive values indicate an upward band bending.

Thickness (nm)	Peak Shift (± 0.05 eV)							
	Mg 1s	Zn 2p	O KLL	O 1s	Zn LMM	Mg KLL	Zn 3p	**BB**
2	0.34	0.32	0.24	0.29	0.34	0.35	0.26	**0.31**
5	N/A	N/A	N/A	0.37	0.41	N/A	0.34	**0.37**
Thickness (nm)	Cd MNN		Te MNN	Cd 3d		Te 3d	Te 4d	**BB**
2	-0.24		-0.21	-0.10		-0.08	-0.10	**-0.13**
5	-0.12		-0.08	-0.05		-0.03	-0.05	**-0.07**

7.4 Electronic Properties

To determine the band edge offsets at the interface, the band edge energies without the influence of the interface are needed. Figure 7.5 displays UPS measurements of the occupied states (left) and IPES measurements of the unoccupied states (right) for the bare substrate and 10 nm thick CdTe film (bottom and top respectively). To determine the band edges a distinction must be drawn between band edge and defect states. For both UPS and IPES the spectral onset will be dominated by the band edge, however if the concentration of defect states is large enough, a "foot" will be present at the spectral onset that cannot be explained by only experimental broadening. The CdTe is expected to be predominately defect free; therefore the conventional linear extrapolation of the spectral onset was used (lines through data). We find the CdTe valence band maximum (VBM) of -0.75 ± 0.15 eV and the conduction band minimum (CBM) of 0.79 ± 0.15 eV, relative to the Fermi level and a band gap of 1.54 ± 0.21 eV. (Zn,Mg)O is considered a transparent conducting oxide, thus charge-transporting states must exist at or near the Fermi level to maintain conductivity. In order to maintain transparency the optically active states must be separated by a large band gap ($\gtrsim$ 2.5 eV). Evaluating the (Zn,Mg)O UPS spectrum a major onset is found at -3.17 ± 0.20 eV with a large foot extending to -1.63 ± 0.20 eV. The spectrum is very similar to previously published results

for ZnO, in which the foot likely contains multiple states and the "true" VBM[60]. Similar

spectral features are found in the IPES spectrum. The major onset is determined to be at

0.85 ± 0.2 eV with a foot extending to 0.33 ± 0.2 eV, w.r.t. the Fermi level.
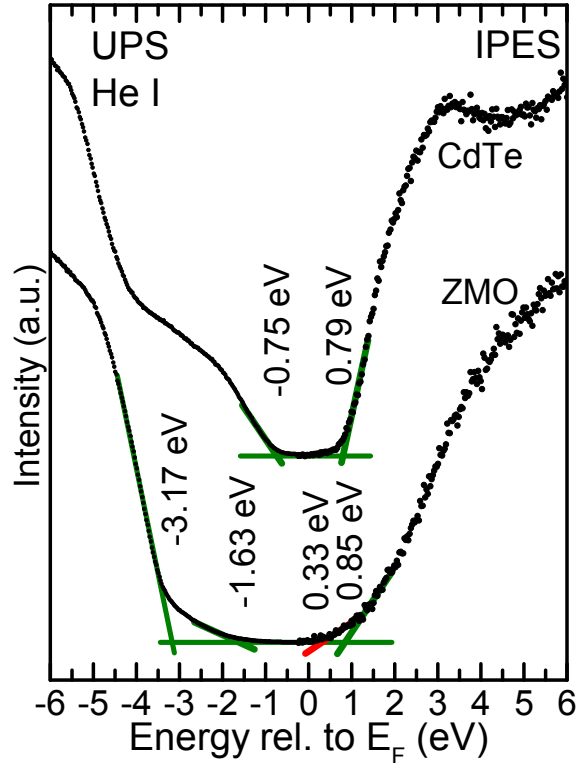
Figure 7.5: UPS (left) and IPES (right) measurements of the 10 nm CdTe film (top) and the bare (Zn,Mg)O substrate (bottom). Linear regions of the leading edges are extrapolated to the baseline in order to determine the CBM and VBM. Green lines indicate optical edges and the red line indicates defect edges.

By combining the UPS, IPES, and band bending information a complete picture

of the electronic level alignment can now be painted, including offsets at the

CdTe/(Zn,Mg)O interface (Figure 7.6). The left side and right side of the image shows

the energy position of band edges for the surface of the bare substrate and thick CdTe

film, respectively. The best determinations for band edges are depicted, as solid green

lines while defect states are dashed red lines. A green box denotes a region that

encompasses the "true" VBM. Diagonal lines depict the band bending determined by

core-level peak shifts. The inferred energy positions (shifted due to band bending) are found in the center of the schematic. An offset of 0.55 eV between like-minded states in the conduction band is found, and flat band conditions are found between the CBM of CdTe in the defect state of (Zn,Mg)O. The valence band offset is found between 0.4 - 1.9 eV.
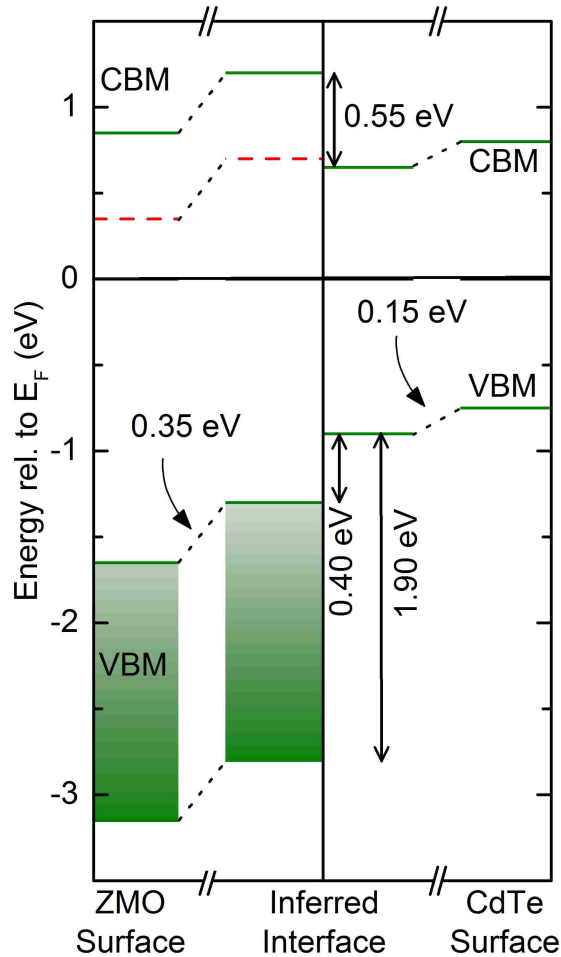
Figure 7.6: Schematic depiction of the interface induced band bending. The left and right side of the depiction represents measured data for the bare substrate and thick CdTe film, left and right respectively. Then a diagonal dashed line denotes bending effects. From this, the inferred interface band edges are drawn in the center. A 0.55 eV electron spike is found at the CBM interface and an energy offset of the VBM is found between 0.4 eV and 1.9 eV. A defect state in the (Zn,Mg)O is found to have no energy offset with the CBM.

7.5 Summary

The chemical and electronic properties of the (Zn,Mg)O/CdTe interface have been studied, with particular emphasis on the electronic level alignment at the interface and replacement of CdS. Zn and Mg are found to diffuse into the CdTe film and form a (Zn, Mg)Te layer at the interface. By combining core level shifts, UPS, and IPES we can infer the electronic level alignment at the interface. By comparing like-minded states in the conduction band a 0.55 eV offsets is found, however flat band conditions exist between the CBM of CdTe and a defect state and (Zn,Mg)O. If there is large enough density of the defect state and sufficient wave function overlap with the CBM of CdTe propagated photoelectrons may be transported through the (Zn,Mg)O film without having to overcome the 0.55 eV energy barrier. A 0.4 - 1.5 eV energy offset is also found at the valence band interface. In conclusion, the electronic level alignment is favorable for device performance only if the (Zn,Mg)O defect state can conduct charges across the (Zn,Mg)O layer.

CHAPTER 8   THE CHEMICAL AND ELECTRONIC STRUCTURE OF

$SnO_2/Zn_{(1-x)}Mg_xO$

8.1 Introduction & Sample Preparation

To continue investigating the chemical and interfacial properties of (Zn,Mg)O, started in Chapter 9, investigation of the window-side interface band alignment was performed. For this study SnO_2 coated glass substrates were coated with 0, 5, and 10 nm of (Zn,Mg)O using ALD. The samples were then removed from the deposition chamber in a N_2-filled glovebag. The samples were immediately vacuum packaged and shipped to UNLV. Upon delivery to UNLV, the samples were immediately moved to an N_2-filled glovebox. To minimize any time-dependent changes of the films, the measurements series was started immediately.

8.2 Chemical Properties

XPS survey spectra of the three surfaces (Fig. 8.1) show photoelectron and Auger lines for all expected elements (Zn, Mg, Sn, and O) are present at the surface. The 0 nm (Zn,Mg)O sample is a bare SnO_2 layer. The 10 nm sample is thick enough to attenuate all emitted electrons from the SnO_2 sublayer and only collect electrons as from the $Zn_{(1-x)}Mg_xO$ layer. The think sample (5 nm) is thick enough to attenuate nearly all of the photoelectrons from the SnO_2 sublayer. In addition we also see small amounts of carbon and Fluorine on all surfaces. Fluorine is present but not seen in the Al K_α survey spectra due overlaying photoelectric and Auger lines, but is seen with Mg K_α excitation (not shown).
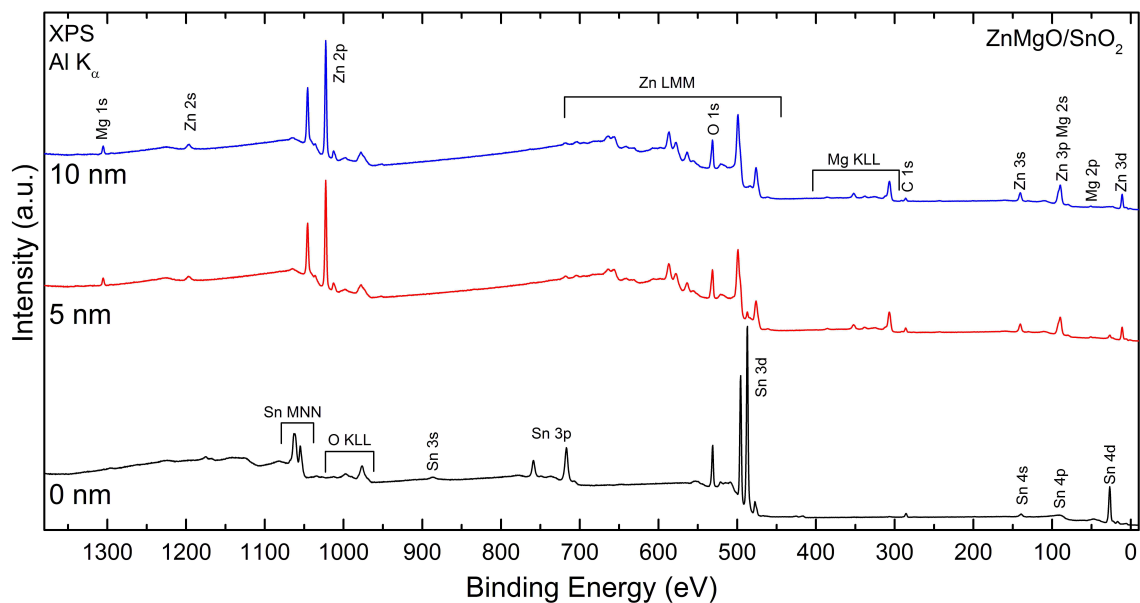
Figure 8.1: Al Kα XPS survey spectra of 0 nm (black), 5 nm (red), and 10 nm (blue) $(Zn,Mg)O/SnO_2$.

To continue evaluating the chemical properties of the interface a close examination of elements expected to be in a metal-oxide chemical environment is performed. Figure 8.2 shows detailed measurements of the most intense photoelectric (left) and Auger (right) peaks for Mg (top), Zn (middle), and Sn (bottom). The "0 nm" sample is expected to be SnO_2, and one would not expect Sn or Mg to be present. Both Sn $3d_{3/2}$ and MNN peaks are strong and consistent with Sn in a SnO_2 chemical environment. The peak centers are near the edge of energies SnO_2 peaks are reported in literature, however this may be explained by downward surface band bending. No Zn is seen on the surface of the "0 nm" film, however weak Mg 1s and KLL signals are seen. Due to the proprietary nature of the sample production the source of the Mg contamination cannot be determined, however the vast majority of the surface is classified as SnO_2.

74
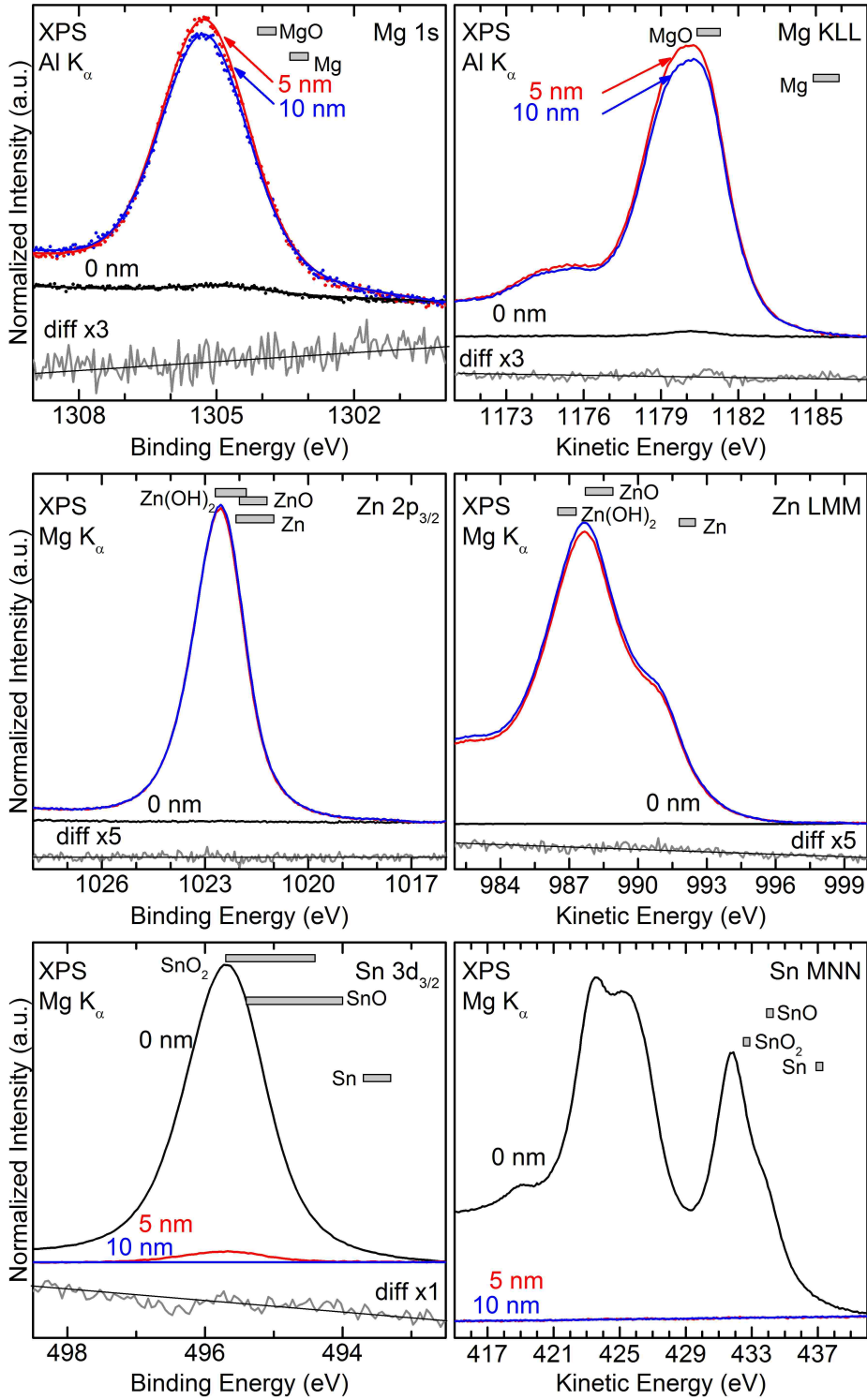
Figure 8.2: Detailed photoelectron and Auger region of expected cation elements, respectively labeled (upper right corner). Ranges of binding/kinetic energies for various species are denoted as grey boxes. The difference of the two most intense peaks, normalized to peak maxima, is plotted below the respective spectra (grey line).

Moving to the intermediate film ("5 nm") one would expect to see SnO_2, MgO, and ZnO to some degree. In fact strong Zn and Mg signal is detected, however the respective peak centers are approx. 1 eV to higher binding energy (low kinetic energy) than the range of reported values for MgO and ZnO. This shift, like in the case of Sn, is likely due to surface band bending. Sn $3d_{3/2}$ intensity is found, but not Sn MNN signal. This may be explained by attenuation of the low energy Auger electrons. Weak Sn signal indicated 5 nm of (Zn,Mg)O is appropriate to study the band edge alignment at the interface. No peak shift is found between "0 nm" and "5 nm," and is confirmed by the difference of the two spectra have no peak-like features, which indicates Sn has not changed chemical environments and no interface induced band bending is seen.

Lastly, the thick sample ("10 nm") MgO and ZnO should be seen but not SnO_2. Mg and Zn are again found in metal oxide chemical environments with the same surface band bending found on the "5 nm" sample. Zn intensity slightly increases as expected for a thicker (Zn,Mg)O film. Mg intensity however, slightly decreases, which indicates a slight change in the Zn/Mg ratio, which cannot be explained by surface adsorbates nor attenuation differences.

To investigate the small amount of fluorine present at the surface of the sample a detailed inspection of the F 1s photoelectric and F KLL peak was needed. Both F 1s and F Auger signals are found to some degree, albeit very weak, on all three samples. The F signal is likely from the F dopant added to the SnO_2 film. F signal is extremely weak for the bare SnO_2 film, as expected for a dopant. With addition of a thin film of (Zn,Mg)O there is a significant increase in F signal, which is then decreased by a thicker film. These intensity variations suggest that F migrates to the SnO_2/(Zn,Mg)O interface and slightly

diffuses into the (Zn,Mg)O film. Any band bending effects caused by the presence of F will be accounted for by analysis of peak shift below.
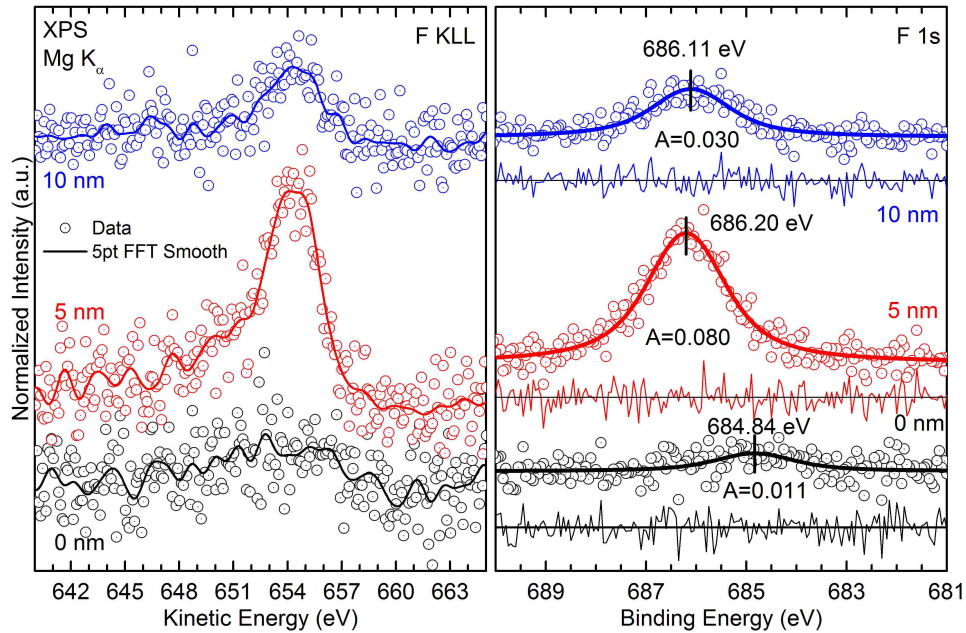
Figure 8.3: XAES and XPS detailed spectra of F KLL (left) and F 1s (right) emissions. F is most prevalent for the 5 nm sample, which suggests (Zn,Mg)O to increase the F diffusion to the interface.

8.3 Electronic properties

As in the case for the CdTe/(Zn,Mg)O interface, the band edges of the bare substrate and thickest overlayer are determined and then adjusted based on band bending to determine the interfacial band alignment. Again a distinction is made between optically active and defect states. Multiple linear regions are found in both the UPS and IPES data (Figure 8.4) that need to be analyzed. The shape of the (Zn,Mg)O data is similar to that seen in Chapter 7, therefore linear extrapolations were performed in the same spectral locations. Energy locations of the linear extrapolation are slightly shifted, which may be due to differences in layer thickness, interfacial (Zn,Mg)Te, dopants/contaminants, and/or stoichiometry. A range of possible valence band maxima

are found ranging -3.7 – -2.3 eV for (Zn,Mg)O and -4.1 – -2.1 eV for SnO_2. Evaluating

the conduction band of the (Zn,Mg)O, the CBM is determined to be 1.4 eV and a defect

state is found at 0.8 eV. The SnO_2 shows similar results where the first major onset is

seen at 1.0 eV. A foot is present prior to the onset that cannot be explained by

experimental broadening, which suggest it is a defect state. Furthermore, two additional

onsets are found at 1.6 eV and 2.3 eV, which may be optical or defect states.
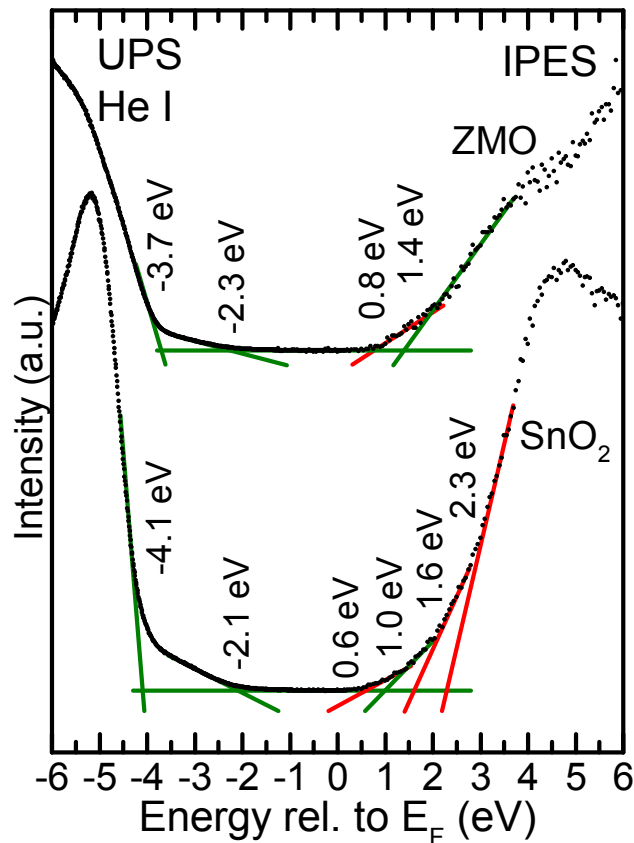
Figure 8.4: UPS (left) and IPES (right) measurements of the 10 nm (Zn,Mg)O film (top) and the bare SnO_2 substrate (bottom). Linear regions of the leading edges are extrapolated to the baseline in order to determine the CBM and VBM. Green lines indicate optical edges and red line indicate defect or other states.

Unlike the CdTe/(Zn,Mg)O interface, no interface induced band bending is observed, therefore the electronic level alignment can be determined directly from surface band edges. Figure 8.5 is a schematic depiction of the electronic level alignment at the $(Zn,Mg)O/SnO_2$ interface. A 0.2 eV offset is found at the interface of "like-minded" states in the valence bands. An electron cliff is seen in the conduction band minima of 0.4 eV, which would not likely be detrimental to the overall performance of the device. In Chapter 7 it was speculated that the defect state in the (Zn,Mg)O can carry charges. Following that hypothesis, an electron spike of 0.2 eV is seen between it and the CBM of the SnO_2.
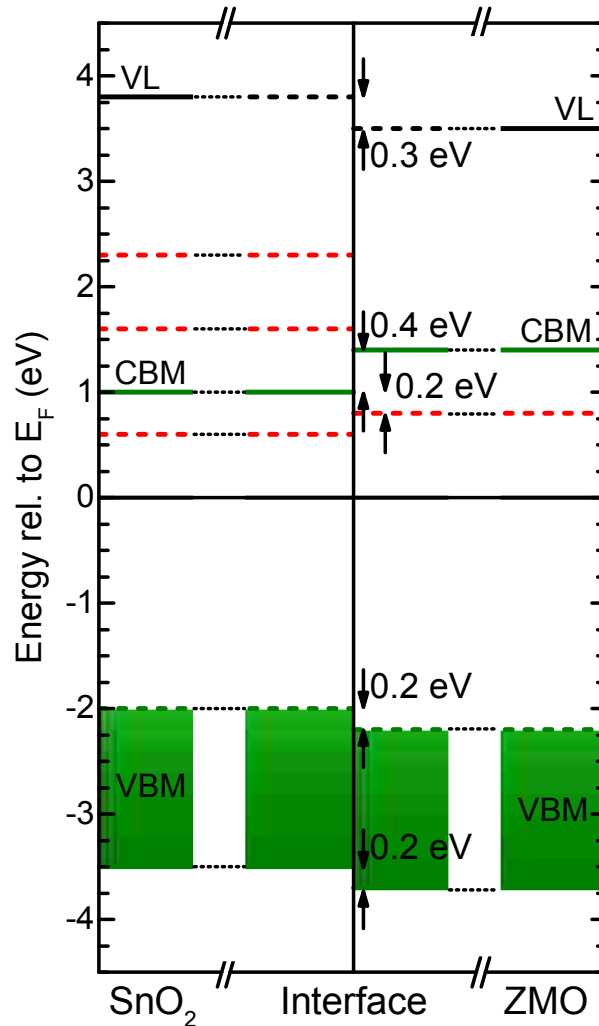
Figure 8.5: Schematic depiction of the interface induced band bending. The left and right side of the depiction represents measured data for the surfaces of the bare SnO_2 and thick (Zn,Mg)O film, left and right, respectively. From this, the inferred interface band edges are drawn in the center. A 0.4 eV electron spike is found at the CBM interface and energy offset at the VBM of 0.2 eV between like-minded states.

8.4 Summary

The chemical and electronic properties of the SnO_2/(Zn,Mg)O interface has been studied, with particular emphasis on the electronic level alignment at the interface and replacement of CdS. (Zn,Mg)O is found to increase the diffusion of the dopant F from the TCO to the surface. By combining core level shifts, UPS, and IPES we can infer the

electronic level alignment at the interface. Comparing like-minded states in the

conduction band a 0.4 eV offset is found. A 0.2 eV energy offset is also found at the

valence band interface between like-minded states.

CHAPTER 9 SUMMARY

In this dissertation, the investigation of surfaces and interfaces in relevant CdTe-based photovoltaic devices was presented. Many complementary analytical techniques, spectroscopic and microscopic, have demonstrated as being effective and insightful tools for device optimizations. The motivation behind this work was to investigate the chemical and electronic properties of materials, which have important applications in CdTe-based devices. Experiments and samples were carefully designed so that a methodical approach to optimize electronic and chemical properties. The goal of this dissertation is to provide new insight and physical explanations for these properties which will aid in the future optimization.

In Chapter 4, the possibility of removing surface oxides and adsorbates with low energy Ar^+ ion treatment steps was investigated. Surface-sensitive XPS data show the removal of oxygen and carbon with increased treatment times and energy. Careful monitoring of the chemical and electronic surface structure of the treated CdTe surface shows no indications for preferential removal of Cd or Te. However, the broadening of core-level spectra points to a treatment-induced roughening of the CdTe surface. Measurements of the surface band gap show an upward shift of the conduction band and a "wider-gap" material between the CdTe absorber and the back contact, which could potentially reduce electron-hole recombination at the back contact interface.

The effects of $CdCl_2$-treatment on diffused species was studied in Chapter 5, by separating the a layer stack at the SnO_2:F/CdS interface. By investigating the morphology it was found that the center of the samples are smooth and an organic layer is present at the interface that is likely due to residual organic cleaning solvents prior to film

deposition. By incorporating a plasma-cleaning step to remove residual organics device fabricators were able to improve device performance.

XPS was used to probe the chemical environment of the interface and significant amounts of diffusion is found at both $SnO_2:F/CdS$ and $CdS/CdTe$ interfaces before and after $CdCl_2$-treatment. Further work is need to determine the extent of these diffused species. However, one can conclude that the simple heterojunction band alignment picture is not sufficient to describe the interactions of the TCO/Buffer/Absorber layers in a CdTe-based photovoltaic device.

In Chapters 6-8, potential replacements for CdS were studied in order to increase the quantum efficiency for photons between 1.4 and 2.4 eV (band gaps of CdTe and CdS). The chemical and electronic structure of CdS:O thin films produced by incorporating O_2 into the Ar gas flow during sputter deposition surfaces were investigated by XPS, while the bulk of the films were studied by XES. The films were found to be mainly comprised of CdS and $CdSO_4$, with small additions of an intermediate $CdSO_x$ (most likely sulfite) species. With increasing oxygen incorporation, $CdSO_4$ is the preferred species, at the expense of CdS, while the content of the intermediate oxide species remains constant. As the oxygen incorporation into the CdS:O films serves several purposes, it is important to understand the composition of such films not just on an atomic level (i.e., composition of Cd, S, and O), but also from the view point of concentration of particular species (i.e., sulfide, sulfate, and intermediate oxide). With such insights, it is now possible to establish suitable models for the CdS:O film properties and their impact on the performance of high-efficiency thin film solar cells. Furthermore,

empirical tailoring towards the optimal balance between the different species can now be quantified and solar cell optimization is thus greatly facilitated.

The chemical and electronic properties of the (Zn,Mg)O/CdTe interface have been studied, with particular emphasis on the electronic level alignment at the interface and replacement of CdS. Zn and Mg are found to diffuse into the CdTe film and form a (Zn, Mg)Te layer at the interface. By combining core level shifts, UPS, and IPES we can infer the electronic level alignment at the interface. By comparing like-minded states in the conduction band a 0.55 eV offsets is found, however flat band conditions exist between the CBM of CdTe and a defect state and (Zn,Mg)O. If there is large enough density of the defect state and sufficient wave function overlap with the CBM of CdTe propagated photoelectrons may be transported through the (Zn,Mg)O film without having to overcome the 0.55 eV energy barrier. A 0.4 - 1.5 eV energy offset is also found at the valence band interface. In conclusion, the electronic level alignment is favorable for device performance only if the (Zn,Mg)O defect state can conduct charges across the (Zn,Mg)O layer.

The chemical and electronic properties of the SnO_2/(Zn,Mg)O interface has been studied, with particular emphasis on the electronic level alignment at the interface and replacement of CdS. (Zn,Mg)O is found to increase the diffusion of the dopant F from the TCO to the surface. By combining core level shifts, UPS, and IPES we can infer the electronic level alignment at the interface. Comparing like-minded states in the conduction band a 0.4 eV offset is found. A 0.2 eV energy offset is also found at the valence band interface between like-minded states.

APPENDIX

LIST OF SYMBOLS AND ABBRIVATIONS

AFM	Atomic force microscopy
BSE	Backscattered electron
CBM	Conduction band maximum
CdS	Cadmium sulfide
CdTe	Cadmium telluride
CSS	Close space sublimation
DOS	Density of states
E_{bin}	Binding energy
E_F	Fermi energy
E_{kin}	Kinetic energy
E_{vac}	Vacuum level
FTO	Fluorinated tin oxide, $SnO_2:F$
HPD	Heated pocket deposition
IIBB	Interface induced band bending
IMFP	Inelastic mean free path
IPES	Inverse photoelectron spectroscopy
PES	Photoemission spectroscopy
PV	Photovoltaic
SE	Secondary electron
SEM	Scanning electron microscopy
TCO	Transparent conducting oxide

UHV	Ultra-high vacuum
UPS	Ultraviolet photoelectron spectroscopy
VBM	Valence band maximum
VL	Vacuum level
XAES	X-ray excited Auger electron spectroscopy
XAS	X-ray absorption spectroscopy
XES	X-ray emission spectroscopy
XPS	X-ray photoelectron spectroscopy
(Zn,Mg)O	Zinc magnesium Oxide, $Zn_{(1-x)}Mg_xO$
Φ	Work function

BIBLIOGRAPHY

(1)   Green, M. A.; Emery, K.; Hishikawa, Y.; Warta, W.; Dunlop, E. D., Solar Cell
        Efficiency Tables (Version 45). *Prog. Photovoltaics* **2015,** *23* (1), 1-9.

(2)   Sites, J. R., Quantification of Losses in Thin-Film Polycrystalline Solar Cells. *Sol.
        Energy Mater. Sol. Cells* **2003,** *75* (1-2), 243-251.

(3)   Wu, X.; Yan, Y.; Dhere, R. G.; Zhang, Y.; Zhou, J.; Perkins, C.; To, B.,
        Nanostructured CdS:O Film: Preparation, Properties, and Application. *Phys.
        Status Solidi C* **2004,** *1* (4), 1062-1066.

(4)   Kephart, J. M.; Geisthardt, R.; Sampath, W. S. *Sputtered, Oxygenated CdS
        Window Layers for Higher Current in CdS/CdTe Thin Film Solar Cells*,
        Photovoltaic Specialists Conference (PVSC), 2012 38th IEEE, 3-8 June 2012;
        2012; pp 854-858.

(5)   Kephart, J. M.; Geisthardt, R. M.; Sampath, W. S., Optimization of CdTe Thin-
        Film Solar Cell Efficiency Using a Sputtered, Oxygenated CdS Window Layer.
        Prog. Photovoltaics **2015**, 10.1002/pip.2578.

(6)   Islam, M. A.; Sulaiman, Y.; Amin, N., A Comparative Study of BSF Layers for
        Ultra-Thin CdS:O/Cdte Solar Cells. *Chalcogenide Lett.* **2011,** *8* (2), 65-75.

(7)   Paudel, N. R.; Grice, C. R.; Xiao, C. X.; Yan, Y. F., The Effects of High
        Temperature Processing on the Structural and Optical Properties of Oxygenated
        CdS Window Layers in CdTe Solar Cells. *J. Appl. Phys.* **2014,** *116* (4), 044506.

(8)   Wu, X.; Dhere, R. G.; Yan, Y.; Romero, M. J.; Zhang, Y.; Zhou, J.; DeHart, C.;
        Duda, A.; Perkins, C.; To, B. *High-Efficiency Polycrystalline CdTe Thin-Film
        Solar Cells with an Oxygenated Amorphous Cds (a-CdS:O) Window Layer*,
        Photovoltaic Specialists Conference, 2002. Conference Record of the Twenty-
        Ninth IEEE, 19-24 May 2002; **2002**; pp 531-534.

(9)   Sze, S. M., *Semiconductor Devices: Physics and Technology, 2nd Ed*. Wiley India
        Pvt. Limited: **2008**.

(10)   Kranz, L.; Gretener, C.; Perrenoud, J.; Schmitt, R.; Pianezzi, F.; La Mattina, F.;
        Blösch, P.; Cheah, E.; Chirilă, A.; Fella, C. M.; Hagendorfer, H.; Jäger, T.;
        Nishiwaki, S.; Uhl, A. R.; Buecheler, S.; Tiwari, A. N., Doping of Polycrystalline
        Cdte for High-Efficiency Solar Cells on Flexible Metal Foil. *Nat Commun* **2013,**
        4.

(11)   Scheer, R.; Schock, H.-W., Thin Film Technology. In *Chalcogenide
        Photovoltaics*, Wiley-VCH Verlag GmbH & Co. KGaA: **2011**, pp 235-275.

(12)   Metzger, W. K.; Albin, D.; Romero, M. J.; Dippo, P.; Young, M., CdCl$_2$ Treatment, S Diffusion, and Recombination in Polycrystalline CdTe. *J. Appl. Phys.* **2006,** *99* (10), 103703.

(13)   McCandless, B. E.; Engelmann, M. G.; Birkmire, R. W., Interdiffusion of CdS/CdTe Thin Films: Modeling X-Ray Diffraction Line Profiles. *J. Appl. Phys.* **2001,** *89* (2), 988-994.

(14)   Soo, J. L.; Huang, S.; Kao, Y. H.; Compaan, A. D., Annealing Effects and Te Mixing in CdTe/CdS Heterojunctions. *Appl. Phys. Lett.* **1999,** *74* (2), 218-220.

(15)   Terheggen, M.; Heinrich, H.; Kostorz, G.; Romeo, A.; Baetzner, D.; Tiwari, A. N.; Bosio, A.; Romeo, N., Structural and Chemical Interface Characterization of CdTe Solar Cells by Transmission Electron Microscopy. *Thin Solid Films* **2003,** *431–432* (0), 262-266.

(16)   McCandless, B. E.; Sites, J. R., Cadmium Telluride Solar Cells. In *Handbook of Photovoltaic Science and Engineering*, John Wiley & Sons, Ltd: **2011**, pp 600-641.

(17)   Gloeckler, M.; Sankin, I.; Zhao, Z., CdTe Solar Cells at the Threshold to 20% Efficiency. *Photovoltaics, IEEE Journal of* **2013,** *3* (4), 1389-1393.

(18)   Chu, T. L.; Chu, S. S.; Britt, J.; Ferekides, C.; Wu, C. Q., Cadmium Zinc Sulfide Films and Heterojunctions. *J. Appl. Phys.* **1991,** *70* (5), 2688-2693.

(19)   Ohtomo, A.; Kawasaki, M.; Koida, T.; Masubuchi, K.; Koinuma, H.; Sakurai, Y.; Yoshida, Y.; Yasuda, T.; Segawa, Y., Mg$_x$Zn$_{1-x}$O as a II–VI Widegap Semiconductor Alloy. *Appl. Phys. Lett.* **1998,** *72* (19), 2466-2468.

(20)   Kephart, J. M.; Geisthardt, R. M.; Sampath, W. S., Optimization of CdTe Thin-Film Solar Cell Efficiency Using a Sputtered, Oxygenated CdS Window Layer. *Prog. Photovoltaics* **2015,** *23* (11), 1484-1492.

(21)   Brigss, D.; P., S. M., *Practical Surface Analysis: Auger and Photoelectron Spectroscopy, 2nd Ed.* John Wiley and Sons: Chichester, **1990**.

(22)   Seah, M. P., Summary of ISO/TC 201 Standard: VII ISO 15472: 2001 - Surface Chemical Analysis - X-Ray Photoelectron Spectrometers - Calibration of Energy Scales. *Surf. Interface Anal.* **2001,** *31* (8), 721-723.

(23)   Schedin, F.; Thornton, G.; Uhrberg, R. I. G., Windows and Photocathodes for a High Resolution Solid State Bandpass Ultraviolet Photon Detector for Inverse Photoemission. *Rev. Sci. Instrum.* **1997,** *68* (1), 41-46.

(24)   Dibeler, V. H.; Walker, J. A.; McCulloh, K. E.; Rosenstock, H. M., Effect of Hot Bands on the Ionization Threshold of Some Diatomic Halogen Molecules. *International Journal of Mass Spectrometry and Ion Physics* **1971,** *7* (3), 209-219.

(25)   Smith, N. V.; Woodruff, D. P., Inverse Photoemission from Metal Surfaces. *Progress in Surface Science* **1986,** *21* (4), 295-370.

(26)   Briggs, D.; Seah, M. P., *Practical Surface Analysis: Auger and Photoelectron Spectroscopy*. 2nd ed. ed.; John Wiley and Sons: Chichester ; New York, **1990**.

(27)   Gleim, T.; Heske, C.; Umbach, E.; Schumacher, C.; Gundel, S.; Faschinger, W.; Fleszar, A.; Ammon, C.; Probst, M.; Steinrück, H. P., Formation of the ZnSe/(Te/)GaAs(100) Heterojunction. *Surface Science* **2003,** *531* (1), 77-85.

(28)   Morkel, M.; Weinhardt, L.; Lohmüller, B.; Heske, C.; Umbach, E.; Riedl, W.; Zweigart, S.; Karg, F., Flat Conduction-Band Alignment at the CdS/CuInSe$_2$ Thin-Film Solar-Cell Heterojunction. *Appl. Phys. Lett.* **2001,** *79* (27), 4482-4484.

(29)   Wojdyr, M., Fityk: A General-Purpose Peak Fitting Program. *J. Appl. Crystallogr.* **2010,** *43*, 1126-1128.

(30)   Shirley, D. A., High-Resolution X-Ray Photoemission Spectrum of the Valence Bands of Gold. *Phys. Rev. B* **1972,** *5* (12), 4709-4714.

(31)   Doniach, S.; Sunjic, M., Many-Electron Singularity in X-Ray Photoemission and X-Ray Line Spectra from Metals. *Journal of Physics C: Solid State Physics* **1970,** *3* (2), 285.

(32)   Attwood, D., *Soft X-Rays and Extreme Ultraviolet Radiation: Principles and Applications*. Cambridge University Press: **2000**.

(33)   Henke, B. L.; Gullikson, E. M.; Davis, J. C., X-Ray Interactions - Photoabsorption, Scattering, Transmission, and Reflection at E: 50-30,000 eV, Z:1-92. *At. Data Nucl. Data Tables* **1993,** *54* (2), 181-342.

(34)   Jia, J. J.; Callcott, T. A.; Yurkas, J.; Ellis, A. W.; Himpsel, F. J.; Samant, M. G.; Stöhr, J.; Ederer, D. L.; Carlisle, J. A.; Hudson, E. A.; Terminello, L. J.; Shuh, D. K.; Perera, R. C. C., First Experimental Results from IBM/Tenn/Tulane/LLNL/ LBL Undulator Beamline at the Advanced Light Source. *Rev. Sci. Instrum.* **1995,** *66* (2), 1394-1397.

(35)   Fuchs, O.; Weinhardt, L.; Blum, M.; Weigand, M.; Umbach, E.; Bar, M.; Heske, C.; Denlinger, J.; Chuang, Y. D.; McKinney, W.; Hussain, Z.; Gullikson, E.; Jones, M.; Batson, P.; Nelles, B.; Follath, R., High-Resolution, High-Transmission Soft X-Ray Spectrometer for the Study of Biological Samples. *Rev. Sci. Instrum.* **2009,** *80* (6), 063103.

(36)   Sampath, W. S.; Kohli, S.; Enzenroth, R. A.; Barth, K. L.; Manivannan, V.; Hilfiker, J.; McCurdy, P. R.; Barricklow, K.; Noronha, P. *Advances in Continuous, in-Line Processing of Stable CdS/CdTe Devices*, Photovoltaic Specialists Conference, 2008. PVSC '08. 33rd IEEE, 11-16 May 2008; **2008**; pp 1-4.

(37)   Kindig, N. B., Effects of Band-Bending on Energy Distribution Curves in Photoemission. *J. Appl. Phys.* **1967,** *38* (8), 3285-&.

(38)   Moulder, J.; Stickle, W.; Sobol, P.; Bomben, K., *Handbook of X-Ray Photoelectron Spectroscopy*. Perkin-Elmer, Physical Electronics Division: Eden Prairie U.S.A.

(39)   Nist X-Ray Photoelectron Spectroscopy Database. http://srdata.nist.gov/xps/.

(40)   Scofield, J. H., Hartree-Slater Subshell Photoionization Cross-Sections at 1254 and 1487 eV. *J. Electron Spectrosc. Relat. Phenom.* **1976,** *8* (2), 129-137.

(41)   Powell, C.; Jablonski, A. *Nist Electron Ienlastic-Mean-Free-Path Databas*, 1.2; National Insititute of Standards and Technology: Gaithersburg, MD, **2010**.

(42)   Bacaksiz, E.; Altunbas, M.; Yflniaz, S.; Tornakin, M.; Parlak, M., Effects of $CdCl_2$ Treatment on Properties of CdTe Thin Films Grown by Evaporation at Low Substrate Temperatures. *Crystal Research and Technology* **2007,** *42* (9), 890-894.

(43)   Bar, M.; Nishiwaki, S.; Weinhardt, L.; Pookpanratana, S.; Fuchs, O.; Blum, M.; Yang, W.; Denlinger, J. D.; Shafarman, W. N.; Heske, C., Depth-Resolved Band Gap in $Cu(In,Ga)(S,Se)_2$ Thin Films. *Appl. Phys. Lett.* **2008,** *93* (24).

(44)   Dhere, R. G.; Asher, S. E.; Jones, K. M.; Al‑Jassim, M. M.; Moutinho, H. R.; Rose, D. H.; Dippo, P.; Sheldon, P., Characterization of Intermixing at the CdS/CdTe Interface in CSS Deposited CdTe. *AIP Conference Proceedings* **1996,** *353* (1), 392-399.

(45)   Fritsche, J.; Klein, A.; Jaegermann, W., Thin Film Solar Cells: Materials Science at Interfaces. *Advanced Engineering Materials* **2005,** *7* (10), 914-920.

(46)   *Phoibos Hemispherical Energy Analyzer Series*. Specs GmbH: **2008**; Vol. 3.1.

(47)   Mahathongdy, Y.; Wolden, C. A.; Baldwin, R. M.; Albin, D. S., *Vapor CdCl₂-Optimization and Screening Experiments for an All Dry Chloride Treatment of Cds/Cdte Solar Cells*. **1998**, p Medium: ED; Size: vp.

(48)   Klenk, R.; Steigert, A.; Rissom, T.; Greiner, D.; Kaufmann, C. A.; Unold, T.;
        Lux-Steiner, M. C., Junction Formation by Zn(O,S) Sputtering Yields CIGSe-
        Based Cells with Efficiencies Exceeding 18%. *Prog. Photovoltaics* **2014,** *22* (2),
        161-165.

(49)   Kartopu, G.; Clayton, A. J.; Brooks, W. S. M.; Hodgson, S. D.; Barrioz, V.;
        Maertens, A.; Lamb, D. A.; Irvine, S. J. C., Effect of Window Layer Composition
        in $Cd_{1-X}Zn_X s$/Cdte Solar Cells. *Prog. Photovoltaics* **2014,** *22* (1), 18-23.

(50)   Naghavi, N.; Abou-Ras, D.; Allsop, N.; Barreau, N.; Bucheler, S.; Ennaoui, A.;
        Fischer, C. H.; Guillen, C.; Hariskos, D.; Herrero, J.; Klenk, R.; Kushiya, K.;
        Lincot, D.; Menner, R.; Nakada, T.; Platzer-Bjorkman, C.; Spiering, S.; Tiwari,
        A. N.; Torndahl, T., Buffer Layers and Transparent Conducting Oxides for
        Chalcopyrite $Cu(in,Ga)(S,Se)_2$ Based Thin Film Photovoltaics: Present Status and
        Current Developments. *Prog. Photovoltaics* **2010,** *18* (6), 411-433.

(51)   Soo, Y. L.; Sun, W. H.; Weng, S. C.; Lin, Y. S.; Chang, S. L.; Jang, L. Y.; Wu,
        X.; Yan, Y., Local Environment Surrounding S and Cd in Cds:O Thin Film
        Photovoltaic Materials Probed by X-Ray Absorption Fine Structures. *Appl. Phys.
        Lett.* **2006,** *89* (13), 131908.

(52)   Blum, M.; Weinhardt, L.; Fuchs, O.; Baer, M.; Zhang, Y.; Weigand, M.; Krause,
        S.; Pookpanratana, S.; Hofmann, T.; Yang, W.; Denlinger, J. D.; Umbach, E.;
        Heske, C., Solid and Liquid Spectroscopic Analysis (SALSA)-a Soft X-Ray
        Spectroscopy Endstation with a Novel Flow-through Liquid Cell. *Rev. Sci.
        Instrum.* **2009,** *80* (12), 123102.

(53)   Weinhardt, L.; Fuchs, O.; Umbach, E.; Heske, C.; Fleszar, A.; Hanke, W.;
        Denlinger, J. D., Resonant Inelastic Soft X-Ray Scattering, X-Ray Absorption
        Spectroscopy, and Density Functional Theory Calculations of the Electronic Bulk
        Band Structure of Cds. *Phys. Rev. B* **2007,** *75* (16), 165207-165211.

(54)   Weinhardt, L.; Fuchs, O.; Fleszar, A.; Baer, M.; Blum, M.; Weigand, M.;
        Denlinger, J. D.; Yang, W.; Hanke, W.; Umbach, E.; Heske, C., Resonant
        Inelastic Soft X-Ray Scattering of CdS: A Two-Dimensional Electronic Structure
        Map Approach. *Phys. Rev. B* **2009,** *79* (16), 165305-165309.

(55)   Meisel, A.; Steuer, I.; Szargan, R., $L_{2,3}$ X-Ray Emission Spectrum of Sulfur in
        Various Compounds. *Spectrochim. Acta, Part B* **1968,** *B 23* (8), 527-529.

(56)   Meisel, A.; Leonhardt, G.; Szargan, R., *Röntgenspektren Und Chemische
        Bindung*. Akademische Verlagsgesellschaft Geest u. Portig: **1977**.

(57)   Reichardt, J.; Bar, M.; Grimm, A.; Kotschau, I.; Lauermann, I.; Sokoll, S.; Lux-
        Steiner, M. C.; Fischer, C. H.; Heske, C.; Weinhardt, L.; Fuchs, O.; Jung, C.;
        Gudat, W.; Niesen, T. P.; Karg, F., Inducing and Monitoring

Photoelectrochemical Reactions at Surfaces and Buried Interfaces in Cu(In,Ga)(S,Se)$_2$ Thin-Film Solar Cells. *Appl. Phys. Lett.* **2005,** *86* (17), 172102.

(58)   Lane, D. W., A Review of the Optical Band Gap of Thin Film CdS$_x$Te$_{1-X}$. *Sol. Energy Mater. Sol. Cells* **2006,** *90* (9), 1169-1175.

(59)   Romeo, N.; Bosio, A.; Canevari, V.; Podesta, A., Recent Progress on CdTe/CdS Thin Film Solar Cells. *Solar Energy* **2004,** *77* (6), 795-801.

(60)   Weinhardt, L.; Heske, C.; Umbach, E.; Niesen, T. P.; Visbeck, S.; Karg, F., Band Alignment at the i-ZnO/CdS Interface in Cu(In,Ga)(S,Se)$_2$ Thin-Film Solar Cells. *Appl. Phys. Lett.* **2004,** *84* (16), 3175-3177.

CURRICULUM VITAE

Graduate College
University of Nevada, Las Vegas
Douglas A. Duncan

Degrees:
Bachelor of Science, Chemistry, 2011
University of Nevada, Las Vegas

Special Honors and Awards:
Outstanding Undergraduate Chemistry Student at UNLV (2011)

Publications:
"Electronic Structure of the Zn(O,S)/Cu(In,Ga)Se$_2$ Thin-Film Solar Cell Interface",
Mezher, M.; Garris, R.; Mansfield, L.; Horsley, K.; Weinhardt, L.; **Duncan, D. A**.; Blum, M.; Rosenberg, S.; Bär, M.; Ramanathan, K.; Heske, C. *Prog. Photovolt.* (submitted).

"Characterization of Sulfur Bonding in CdS:O Buffer layers for CdTe-Based Thin-Film Solar Cells",
Duncan D. A.; Kephart J. M.; Horsley K.; Blum M.; Mezher M.; Weinhardt L.; Häming M.; Wilks R. G.; Hofmann T.; Yang W.; Bär M.; Sampath W. S.; Heske C. *ACS Appl. Mater. Interfaces*, **7**, 16382 (2015)

"Impact of Annealing on the Chemical Structure and Morphology of the Thin-Film CdTe/ZnO Interface",
Horsley K.; Beal R. J.; Wilks R. G.; Blum M.; Häming M.; **Hanks D. A.**; Weir M. G.; Hofmann T.; Weinhardt L.; Bär M.; Potter Jr. B. G.; Heske C. *J. Appl. Phys*., **116**, 024312 (2014)

"Photoemission Study of CdTe Surfaces After Low-Energy Ion Treatment",
Hanks, D.; Weir, M.; Horsley, K.; Hofmann, T.; Weinhardt, L.; Bär, M.; Barricklow, K.; Kobyakov, P.; Sampath, W.; Heske, C. Photovoltaic Specialists Conference (PVSC), 2012 38th IEEE, 3-8 June 2012; **2012**, 396-399

"Chemical Surface and Interface Properties of Differently-Stressed (Au/Cu/)CdTe/CdS Thin-Film Solar Cell Structure",
Horsley, K.; Wilks, R.; **Hanks, D.**; Blum, M.; Paudel, N.; Compaan, A.; Yang, W.; Bär, M.; Weinhardt, L.; Heske, C. Photovoltaic Specialists Conference (PVSC), 2012 38th IEEE, 3-8 June 2012; **2012**, 400-405

Dissertation Title:
  Chemical and Electronic Structure of Surface and Interfaces in Cadmium Telluride
  Photovoltaic Devices
Dissertation Examination Committee:
  Chairperson, Clemens Heske, Dr. rer. Nat.
  Committee Member, Kathleen Robins, Ph. D.
  Committee Member, Dong-Chan Lee, Ph. D.
  Graduate Faculty Representative, Rama Venkat, Ph. D.